UCLA
UCLA Previously Published Works

Title
Determining EMIC Wave Vector Properties Through Multi-Point Measurements: The Wave Curl Analysis

Permalink
https://escholarship.org/uc/item/93c2x04h

Journal
Journal of Geophysical Research Space Physics, 126(4)

ISSN
2169-9380

Authors
Vines, SK
Anderson, BJ
Allen, RC
et al.

Publication Date
2021-04-01

DOI
10.1029/2020ja028922

Peer reviewed

Key Points:
- The wave curl analysis is a new implementation of determining **k** using observed wave magnetic field and associated current density
- The wave curl analysis reliably determines **k** for both synthetic waves and Magnetospheric MultiScale observations of electromagnetic ion cyclotron waves
- The calculated **k** is robust relative to time and frequency ranges used in the analysis, and agrees well with linear dispersion theory

Correspondence to:
S. K. Vines,
sarah.vines@jhuapl.edu

Determining EMIC Wave Vector Properties Through Multi-Point Measurements: The Wave Curl Analysis

S. K. Vines[1] , B. J. Anderson[1] , R. C. Allen[1] , R. E. Denton[2] ,
M. J. Engebretson[3] , J. R. Johnson[4] , S. Toledo-Redondo[5] , J. H. Lee[6] , D. L. Turner[1] ,
R. E. Ergun[7] , R. J. Strangeway[8] , C. T. Russell[8] , H. Wei[8] , R. B. Torbert[9,10] ,
S. A. Fuselier[10,11] , B. L. Giles[12] , and J. L. Burch[10]

[1]The Johns Hopkins University Applied Physics Laboratory, Laurel, MD, USA, [2]Department of Physics and Astronomy, Dartmouth College, Hanover, NH, USA, [3]Department of Physics, Augsburg University, Minneapolis, MN, USA, [4]Department of Engineering, Andrews University, Berrien Springs, MI, USA, [5]Department of Electromagnetism and Electronics, University of Murcia, Murcia, Spain, [6]The Aerospace Corporation, El Segundo, CA, USA, [7]Laboratory for Atmospheric and Space Physics, University of Colorado at Boulder, Boulder, CO, USA, [8]Department of Earth, Planetary, and Space Sciences, Institute for Geophysics and Planetary Physics, University of California at Los Angeles, Los Angeles, CA, USA, [9]Space Science Center, University of New Hampshire, Durham, NH, USA, [10]Southwest Research Institute, San Antonio, TX, USA, [11]Department of Physics and Astronomy, University of Texas at San Antonio, San Antonio, TX, USA, [12]NASA Goddard Space Flight Center, Greenbelt, MD, USA

Abstract Electromagnetic ion cyclotron (EMIC) waves play important roles in particle loss processes in the magnetosphere. Determining the evolution of EMIC waves as they propagate and how this evolution affects wave-particle interactions requires accurate knowledge of the wave vector, **k**. We present a technique using the curl of the wave magnetic field to determine **k** observationally, enabled by the unique configuration and instrumentation of the Magnetospheric MultiScale (MMS) spacecraft. The wave curl analysis is demonstrated for synthetic arbitrary electromagnetic waves with varying properties typical of observed EMIC waves. The method is also applied to an EMIC wave interval observed by MMS on October 28, 2015. The derived wave properties and **k** from the wave curl analysis for the observed EMIC wave are compared with the Waves in Homogenous, Anisotropic, Multi-component Plasma (WHAMP) wave dispersion solution and with results from other single- and multi-spacecraft techniques. We find good agreement between **k** from the wave curl analysis, **k** determined from other observational techniques, and **k** determined from WHAMP. Additionally, the variation of **k** due to the time and frequency intervals used in the wave curl analysis is explored. This exploration demonstrates that the method is robust when applied to a wave containing at least 3–4 wave periods and over a rather wide frequency range encompassing the peak wave emission. These results provide confidence that we are able to directly determine the wave vector properties using this multi-spacecraft method implementation, enabling systematic studies of EMIC wave **k** properties with MMS.

Plain Language Summary Waves generated within space plasmas play important roles in accelerating, heating, and depleting charged particles in Earth's magnetosphere. The wave vector, **k**, mathematically relates the wavelength, direction of wave motion, and wave type to the conditions that produced it. This also tells us if a wave can interact with electrons and ions in ways that will affect the radiation belts. A key problem in understanding waves in space is that **k** is very difficult to determine observationally. We present a method for calculating **k** using Magnetospheric Multiscale (MMS) mission data. The "wave curl analysis" uses magnetic field measurements from all four MMS spacecraft to determine the electric current of the magnetic field fluctuations, which allows for direct calculation of **k**. We test the method on mathematically generated waveforms with properties that mimic electromagnetic ion cyclotron (EMIC) waves previously observed by MMS. We then applied this method to EMIC wave observations and compared the results to theoretical predictions and other methods for estimating **k** from spacecraft measurements. The wave curl analysis opens up a new way to use MMS to understand how EMIC waves are generated, how they travel and evolve, and how they affect plasma in the near-Earth space environment.

1. Introduction

Electromagnetic ion cyclotron (EMIC) waves are an important category of waves that frequently occurs in space plasmas (e.g., Allen et al., 2015; Anderson et al., 1992a; Denton, Gary, et al., 1994; Isenberg, 1984; Kim et al., 2015; Min et al., 2012). These waves act to limit the hot ion anisotropy that drives them (Gary & Lee, 1994; Kennel & Petschek, 1966; Rauch & Roux, 1982). For the Earth's magnetosphere in particular, these waves subsequently interact with the local plasma to pitch-angle scatter energetic ions and relativistic electrons, leading to depletion of the outer radiation belts and ion precipitation during geomagnetically active times (e.g., Cornwall, 1965; Engebretson et al., 2015; Horne & Thorne, 1997; Jordanova et al., 2008; Thorne & Kennel, 1971; Ukhorskiy et al., 2010; Yahnin & Yahnina, 2007). These waves also resonantly heat low-energy, heavy ions (e.g., Kitamura et al., 2018; Rauch & Roux, 1982; Zhang et al., 2010).

In standard plasma wave theory, where the wavefield is described as a plane wave, $\delta \mathbf{B}_w(\mathbf{r},t) = \delta \mathbf{B} \exp(i(\mathbf{k} \cdot \mathbf{r} - \omega t))$ (where $\delta \mathbf{B}$ is the wave amplitude, ω is the wave angular frequency, t is time, $\mathbf{k}$ is the wave vector, and $\mathbf{r}$ is the spatial coordinate), EMIC waves are generated as transverse, left-hand polarized waves propagating along the background magnetic field. The generation and propagation of EMIC waves in a multi-ion plasma is governed by the plasma dispersion relation, which for parallel propagation in the cold plasma regime is given by Summers & Thorne, 2003.

$$\frac{c^2 k^2}{\omega^2} = 1 - \frac{\omega_{pe}^2}{\omega(\omega + \Omega_e)} - \sum_s \frac{\omega_{ps}^2}{\omega(\omega + \Omega_s)} \tag{1}$$

where s denotes the ion species in the multi-ion plasma (e.g., H^+, He^+, and O^+), k is the wave number, $\omega_{pe} \equiv (4\pi e^2 N_e/m_e)^{1/2}$ is the electron plasma frequency (where N_e is the electron density, m_e the electron mass, and e is the elementary charge), $\omega_{ps} \equiv (4\pi Z_s^2 e^2 N_s/m_s)^{1/2}$ is the ion plasma frequency for ion species s (where Z_s is the species charge normalized to e, and N_s is the ion species density), $\Omega_e \equiv eB_0/(m_e c)$ is the electron cyclotron frequency (where B_0 is the background magnetic field magnitude, and c is the speed of light in a vacuum), and $\Omega_s \equiv Z_s eB_0/(m_s c)$ is the ion cyclotron frequency for ion species s (see also Gomberoff & Neira, 1983; Stix, 1992) (for a more generalized dispersion relation that includes warm plasma components, see Summers and Thorne [2003] and Chen et al. [2011]).

Global modeling efforts incorporating the effect of EMIC waves on inner magnetospheric particle dynamics have generally assumed the EMIC waves in the simulations have $\mathbf{k}$ purely parallel to the background magnetic field, $\mathbf{B}_0$, since the wave growth rate is generally maximized for parallel propagation (e.g., Chen et al., 2009). However, previous observations have found that this assumption is not always true, and that there may be a dependence on the background plasma composition that could lead to preferred growth for EMIC waves with more oblique wave vectors (Allen et al., 2015; Anderson et al., 1992b; Denton et al., 1992; Hu et al., 2010; J. H. Lee et al., 2019; Min et al., 2012). Recent simulations have shown that wave-particle interactions and EMIC wave propagation depend on the orientation of $\mathbf{k}$ relative to $\mathbf{B}_0$ and its transverse gradient, $\nabla_\perp(B_0)$ (e.g., Denton, 2018; Kim & Johnson, 2016). The interaction with relativistic electrons, widely recognized as an important loss process for the Earth's outer radiation belt (e.g., Thorne, 2010; Yuan et al., 2018), also depends sensitively on the orientation of $\mathbf{k}$ and is much more effective for oblique waves, when $\mathbf{k}$ is substantially oblique to the background magnetic field (e.g., D.-Y. Lee et al., 2018). The group velocity, $\partial\omega/\partial\mathbf{k}$, determines the wave propagation direction, and the orientation of $\mathbf{k}$ relative to $\mathbf{B}_0$ is critical in determining whether the waves are guided by the magnetic field and in determining how they interact with ions and electrons (e.g., Johnson & Cheng, 1999; D.-Y. Lee et al., 2018; Thorne & Horne, 1994). Changes in the direction of $\mathbf{k}$ as the EMIC waves propagate can alter resonance conditions and interactions with the local ambient plasma as propagation varies (Chen et al., 2011; Kim & Johnson, 2016). Additionally, recent modeling of the effects of oblique EMIC wave vectors on radial diffusion suggests that even modestly oblique wave vectors can have a non-negligible effect on the resonance conditions and interactions with energetic plasma in the inner magnetosphere. Specifically, modestly oblique EMIC waves can affect the extent of trapping and/or gyrophase bunching, as well as the size of the loss cone, for MeV electrons in the radiation belts (B. Wang et al., 2016).

A major limitation for probing EMIC wave resonant interactions is that the wave vector is profoundly difficult to determine observationally. Prior studies relied largely on minimum variance analysis (MVA) using a single-spacecraft (e.g., Wang et al., 2017). Single-spacecraft MVA techniques provide estimates of the wave normal angle (the angle between $\mathbf{k}$ and the background magnetic field, $\mathbf{B}_0$) (see Means, 1972; Russell et al., 2016; Samson & Olson, 1980), although this is an ambiguous measure, since there is no preserved sign from the calculation (i.e., the wave normal angle from MVA only ranges from 0° to 90° rather than 0° to 180°). Additionally, the use of MVA provides no information on the magnitude of $\mathbf{k}$ (see Appendix 4.4 of Russell et al., 2016), which is important for determining resonance conditions and comparing to the theoretical dispersion relation. Another key problem for single-spacecraft MVA estimates is that the observed waves can actually be the result of a superposition of multiple wave packets, which can result in large errors in the wave normal angle (Anderson et al., 1996; Denton et al., 1996; J. H. Lee & Angelopoulos, 2014). Distinct from MVA, a theoretical method based on Ampere's law has also been devised that uses the wave magnetic field and current density to determine $\mathbf{k}$ (Bellan, 2012; 2016). The approach of Bellan (2016) shows promise, as evidenced by its application to kinetic Alfvén waves in the magnetosheath by Gershman et al. (2017).

With the advent of multi-spacecraft missions (e.g., Cluster, THEMIS, Van Allen Probes, Magnetospheric Multiscale [MMS]), the wave telescope technique (Glassmeier et al., 2001) and the phase differencing method (Balikhin & Gedalin, 1993) were developed to better determine wave vector properties. Both techniques rely on timing between wave packets observed by the individual spacecraft in the constellation. However, spacecraft separations for multi-spacecraft missions prior to MMS, specifically Cluster as that mission progressed, have been so large that the spacecraft typically did not observe the same wave packet. This is problematic because the wave packets may be spatially aliased by one or more wavelengths (see Allen et al., 2013; Pinçon & Motschmann, 1998), making these techniques difficult to use. Since previous multi-spacecraft missions were generally separated by scales much larger than the characteristic size of the individual wave packets, to date, there have been only a handful of case studies utilizing the wave telescope or phase differencing techniques to determine $\mathbf{k}$ (e.g., Allen et al., 2013; Broughton et al., 2008; J. H. Lee et al., 2019; Pakhotin et al., 2013; Turner et al., 2017). Because of the limitations of single-spacecraft MVA techniques and previous multi-spacecraft techniques, the actual wave vector properties of EMIC waves have yet to be systematically determined. Here, we present a method that takes advantage of the configuration and capabilities of the MMS spacecraft to observationally determine the wave vector components of EMIC waves. This method enables future, more accurate and systematic, study of EMIC wave vector properties from MMS observations.

2. Determining k: The Wave Curl Analysis

The key for EMIC wave analysis is that $\nabla \times \mathbf{B}$ provides a way to determine the wave vector. Writing the wavefield, $\delta \mathbf{B}_w$, as

$$\delta \mathbf{B}_w = \delta \mathbf{B} \exp\left(i\left(\mathbf{k}\cdot\mathbf{r} - \omega t\right)\right) \tag{2}$$

and applying Ampere's law, one has

$$\nabla \times \delta \mathbf{B}_w = \mu_0 \delta \mathbf{J}_w = i\mathbf{k} \times \delta \mathbf{B}_w \tag{3}$$

where $\delta \mathbf{J}_w$ (referred to in this paper as the wave-associated current density) is calculated from the curl of $\mathbf{B}$ and so denotes the sum of the charge flow plus displacement currents associated with $\delta \mathbf{B}_w$. Crossing both sides of Equation 3 with the conjugate of the wavefield, $\delta \mathbf{B}_w^*$,

$$\delta \mathbf{B}_w^* \times \mu_0 \delta \mathbf{J}_w = \delta \mathbf{B}_w^* \times \left(i\mathbf{k} \times \delta \mathbf{B}_w\right) \tag{4}$$

Using the identity $\nabla\cdot\delta \mathbf{B}_w = i\mathbf{k}\cdot\delta \mathbf{B}_w = 0 = -i\mathbf{k}\cdot\delta \mathbf{B}_w^*$ (where $\mathbf{k}$ is assumed to be a real-valued vector) and then rearranging terms, Equation 4 can be written in the form of a direct expression for $\mathbf{k}$ as

$$\mathbf{k} = -i\mu_0 \frac{\left(\delta\mathbf{B}_w^* \times \delta\mathbf{J}_w\right)}{|\delta\mathbf{B}_w|^2} \tag{5}$$

When applying Equation 5 to observations, the complex spectral components are obtained from Fourier transforms of the wave magnetic field and wave-associated current density time series data. These components are then directly used in an expanded cross product in the right-hand side,

$$\mathbf{k} = i\mu_0 \frac{\left(\delta\mathbf{J}_w \times \delta\mathbf{B}_w^*\right)}{|\delta\mathbf{B}_w|^2} = i\mu_0 \frac{\left(\mathbf{j}_R + i\mathbf{j}_I\right) \times \left(\mathbf{b}_R - i\mathbf{b}_I\right)}{|\delta\mathbf{B}_w|^2} \tag{6}$$

where the subscripts R and I denote the real and imaginary parts, respectively, of the complex wave fields. The expression in Equation 6 assumes that $\mathbf{k}$ is a real-valued vector that is a function of ω through the frequency dependence of the amplitudes of $\delta\mathbf{J}_w$ and $\delta\mathbf{B}_w$. This treatment is generally valid for weakly dissipative mediums, where $\Re(\mathbf{k}) >> \Im(\mathbf{k})$. Implicit in the use of Equation 2, the expression for $\mathbf{k}$ in Equation 6 also assumes that the wave is characterized by a single $\mathbf{k}$ for each ω. If there is a superposition of waves with the same frequency but different phase (e.g., Denton et al., 1996), the derivation above is valid if the constituent waves have the same $\mathbf{k}$. This approach to determining $\mathbf{k}$ via the application of Ampere's law is also detailed in Bellan (2012, 2016).

For monochromatic, narrow-band waves like EMIC waves, the important range in frequency space for determining $\mathbf{k}$ is the frequency range where the wave power is enhanced. In principle, $\mathbf{k}$ can be evaluated at all frequencies in the domain used for the Fourier analysis of the wave fields. However, wildly varying and erroneous values, arising from noise in the data, can result where there is little wave power (i.e., noise that is amplified by small values of the $|\delta\mathbf{B}_w|^2$ term in the denominator of Equation 6). Additionally, broadband noise at lower frequencies, frequently observed in the magnetosphere, or artificial signals such as spin-tones or emissions from spacecraft heaters and gyros, can lead to erroneous $\mathbf{k}$ determination when not applying a frequency filter. To obtain the predominant $\mathbf{k}$, we calculate a weighted average over the frequency domain, using the magnitude of $\delta\mathbf{J}_w \times \delta\mathbf{B}_w^*$ as the weight. That is,

$$\mathbf{k}_{av} = \frac{\sum_\omega \mathbf{k}_\omega \, |\delta\mathbf{J}_w \times \delta\mathbf{B}_w^*|_\omega}{\sum_\omega |\delta\mathbf{J}_w \times \delta\mathbf{B}_w^*|_\omega}. \tag{7}$$

The wave-associated current density, $\delta\mathbf{J}_w$, can be computed using single or multi-spacecraft techniques, as long as the wave-associated current density is obtained reliably and with a high enough time cadence. In this analysis, multi-point magnetic field observations are needed for using the curlometer technique (Dunlop & Eastwood, 2008; Dunlop et al., 1988, 2002) to obtain the current density, as the configuration of the MMS spacecraft in a tightly spaced (tens of km average inter-spacecraft separation at apogee), nearly regular tetrahedron for much of the mission, is ideally suited for techniques relying on multi-point measurements of gradients in a field (see e.g., Robert et al., 1998). For MMS, the tetrahedron quality factor, ranging from 0 to 1 (where 1 indicates a perfect regular tetrahedron [see Fuselier et al., 2016]), is generally above 0.5 in the regions where EMIC waves have been observed.

The underlying approach of the wave curl analysis is similar to that of Bellan (2016), in that the spectral wave fields are used to solve for $\mathbf{k}$ through application of Ampere's law. However, as will be seen in application of the wave curl analysis to spacecraft measurements, the implementation differs from the method of Bellan (2012, 2016), particularly in the treatment of the individual $\delta\mathbf{B}_w$ and $\delta\mathbf{J}_w$ components, and the weighting of $\mathbf{k}(\omega)$ to arrive at a single, predominant $\mathbf{k}$ for narrow-band emission. Specifically, Bellan (2016) calculates the time-averaged cross-correlation between the $\mathbf{B}$ and $\mathbf{J}$ time series and then applies a Fourier transform, where the simplifying assumption has been made that the position argument is set to 0 (see Equations 13 and 23 of Bellan (2016)). In the analysis presented here, no such assumption of the position is made, and the Fourier transforms are applied first to the time series data so that the cross-product terms are evaluated directly in the spectral domain. Similar to Bellan (2012, 2016), the wave curl analysis can also be conducted as a single-spacecraft technique using plasma moments to calculate the current density.

However, with MMS the high-rate plasma data needed for accurate current density measurements is downlinked only for select collection periods, whereas the magnetometer data at a sufficient time resolution is always available for background fields below 8,000 nT magnitude (Fuselier et al., 2016; Torbert et al., 2016). Given constraints on MMS mission operations, the current density calculated from the curlometer technique at high enough fidelity for this analysis is much more widely available than single-spacecraft plasma moments with the required resolution.

3. Testing the Wave Curl Analysis With Synthetic Wave Packets

The implementation of the wave curl analysis is demonstrated through the application of the method to several synthetic wave packets. To create the synthetic wave data, we define an arbitrary ω and $\mathbf{k}$ without assumption of any particular dispersion relation. This can be done without loss of generality, as the synthetic data are used only to show the accuracy of the wave curl analysis to resolve an ω and $\mathbf{k}$ for a given a wave packet, regardless of the dispersion relation that may have generated the particular wave. After defining ω and $\mathbf{k}$, the electric field is computed from (e.g., Jackson, 1999)

$$\mathbf{E}(\mathbf{r},t) = E_0(\boldsymbol{\varepsilon}_1 + i\boldsymbol{\varepsilon}_2)e^{(i\mathbf{k}\cdot\mathbf{r} - i\omega(t+\phi))} \tag{8}$$

where $\boldsymbol{\varepsilon}_1$ and $\boldsymbol{\varepsilon}_2$ are ellipticity vectors, $E_0 = 1$, and ϕ is a constant phase offset. All polarization states are allowed by varying the direction and magnitude of the ellipticity vectors. As a specific example, to generate a left-handed, circularly polarized wave, $\boldsymbol{\varepsilon}_1$ and $\boldsymbol{\varepsilon}_2$ are chosen to be perpendicular to $\mathbf{k}$, with $|\boldsymbol{\varepsilon}_1| = |\boldsymbol{\varepsilon}_2| = 1$. The magnetic field is then obtained by

$$\mathbf{B}(\mathbf{r},t) = \sqrt{\mu_0 \varepsilon_0} \frac{\mathbf{k} \times \mathbf{E}}{|\mathbf{k}|} \tag{9}$$

Finally, to compute the current density associated with the wave,

$$\mathbf{J}(\mathbf{r},t) = \frac{i\mathbf{k} \times \mathbf{B}}{\mu_0} \tag{10}$$

Equations 8–10 provide the electric field, magnetic field, and current density associated with a wave at a given frequency and wave vector. Multiple waves are generated to represent effects of superposition using different ϕ, $\mathbf{k}$, and ω, between constituent packets such that the wave packets in the time domain overlap. In order to represent time-dependent wave amplitudes, a multiplicative factor in the form of $\cos(t)$ is applied to the wave fields, such that the wave amplitude is seen to grow to a maximum value and then smoothly decay after several wave periods at the peak amplitude. The synthetic magnetic fields are resampled to the resolution of fast-survey mode measurements from the Fluxgate Magnetometers (FGM) on MMS (16 vectors/s) (Russell et al., 2016). The synthetic current density waveforms represent observations from MMS when using curlometer to obtain $\mathbf{J}$, as the current density derived from the curlometer technique is a single vector quantity evaluated at the barycenter of the spacecraft constellation (Dunlop et al., 1988, 2002). The input synthetic magnetic field and current density data are then used to test the accuracy of the wave curl analysis and its performance for different wave normal angles, ambient noise, and superposed wave packets.

Several synthetic wave packets, with some composed of two superposed packets, are generated for differing contributions of the $\mathbf{k}$ components and various wave ellipticities (ε). Random noise is added to the complete timeseries. Table 1 lists the $\mathbf{k}$, ε, frequency in Hz (f), and the difference in phase between constituent waves ($\Delta\phi$) used for the synthetic wave fields displayed in Figure 1. Each of the $\mathbf{k}$ components are in magnetic field-aligned coordinates ($k_{\perp 1}$, $k_{\perp 2}$, $k_{\parallel}$) and are normalized to give $|\mathbf{k}| = 10^{-3}$ rad/km for each wave packet. A total packet duration of 41 s and a frequency of $f = 0.3$ Hz is used for each packet, consistent with EMIC waves observed in the outer magnetosphere by Vines et al. (2019) and with an observed EMIC wave discussed in Section 4.1. Three of the synthetic wave packets (5, 6, 7) are the result of overlapping two constituent packets with different phases and $\mathbf{k}$ directions, which represent simplified cases of the kind of wave superposition that may be seen in observations. The final synthetic packet (9) also consists of two waves, but

Table 1
Synthetic Wave Data Inputs and Wave Curl Analysis Results

Trial #	Input wave parameters									Calculated wave parameters				
	k_1^a [rad/km]	θ_{k1} [°]	ε_1	f_1 [Hz]	k_2^a [rad/km]	$\theta_{k2}0$[°]	ε_2	f_2 [Hz]	$\Delta\phi$ [°]	k_{av}^b [rad/km]	$\theta_{k,av}^c$ [°]	$\theta_{k,MVA}$ [°]	ε (MVA)	$f_{peak,av}$ [Hz]
1	$(0, 0, 1) \times 10^{-3}$	0	−1	0.3	–	–	–	–	–	-3.436×10^{-7} -7.994×10^{-6} 1.010×10^{-3}	0.45	0.443	−0.71	0.324
2	$(1, 0, 1) \times \times 10^{-3}/\sqrt{2}$	45	−1	0.3	–	–	–	–	–	$7,000 \times 10^{-4}$ 2.979×10^{-6} 7.072×10^{-4}	44.7	44.9	−0.50	0.323
3	$(1, 1, 1) \times 10^{-3}/\sqrt{3}$	55	−1	0.3	–	–	–	–	–	5.872×10^{-4} 5.828×10^{-4} 5.745×10^{-4}	55.2	55.1	−0.59	0.326
4	$(1, 0, 0) \times 10^{-3}$	90	−1	0.3	–	–	–	–	–	1.015×10^{-3} 3.312×10^{-6} 3.103×10^{-6}	89.8	89.8	−0.01	0.322
5a,b	$(0, 0, 1) \times 10^{-3}$	0	−1	0.3	$(0, 0, 1) \times 10^{-3}$	0	−1	0.3	90	8.606×10^{-7} 4.695×10^{-6} 1.003×10^{-3}	0.27	0.372	−0.71	0.322
6a,b	$(0, 0, 1) \times 10^{-3}$	0	−1	0.3	$(1, 0, 1) \times 10^{-3}/\sqrt{2}$	45	−1	0.3	0	3.735×10^{-4} -1.509×10^{-4} 9.036×10^{-4}	24.0	23.9	−0.61	0.323
7a,b	$(0, 0, 1) \times 10^{-3}$	0	−1	0.3	$(1, 0, 1) \times 10^{-3}/\sqrt{2}$	45	−1	0.3	90	3.772×10^{-4} 1.596×10^{-4} 9.111×10^{-4}	24.2	23.9	−0.62	0.323
8	$(0, 0, 1) \times 10^{-3}$	0	1	0.3	–	–	–	–	–	1.294×10^{-5} 1.357×10^{-5} 9.963×10^{-4}	1.1	1.52	0.67	0.323
9a,b	$(0, 0, 1) \times 10^{-3}$	0	−1	0.3	$(1, 0, 1) \times 10^{-3}/\sqrt{2}$	45	−1	0.66	0	-7.171×10^{-6} -1.233×10^{-5} 9.968×10^{-4}	0.82	0.657	−0.71	0.325
										7.051×10^{-4} -5.354×10^{-6} 7.0313×10^{-4}	45.2	45.3	−0.51	0.686

[a]The $\mathbf{k}_1$, $\mathbf{k}_2$ components are normalized to produce $|\mathbf{k}_{1,2}| = 10^{-3}$ rad/km (e.g., Trial 2 input is $\mathbf{k}_1 = (7.071 \times 10^{-4}, 0, 7.071 \times 10^{-4})$ rad/km). [b]$\mathbf{k}_{av}$ is calculated from Equation 6. [c]Wave normal angle from the wave curl analysis, $\theta_{k,av} = \tan^{-1}\left(k_\perp / k_\parallel\right)$, where $k_\perp = \sqrt{k_{\perp1}^2 + k_{\perp2}^2}$.

generated using two different frequencies (marked by the horizontal, white-dashed lines in Figures 1d–1h), with one packet at $f = 0.3$ Hz (9a) and the other at $f = 0.66$ Hz (9b). Packets 9a and 9b represent cases when waves in multiple bands (i.e., H⁺-band and He⁺-band) are present. These packets are generated to illustrate a sample of the various types of wave properties expected within the magnetosphere.

The real part of the $\delta\mathbf{B}_w$, $\delta\mathbf{E}_w$, and $\delta\mathbf{J}_w$ waveforms are shown in Figures 1a–1c, along with their corresponding power spectral densities, $P_f(\delta\mathbf{B}_w)$, $P_f(\delta\mathbf{E}_w)$, and $P_f(\delta\mathbf{J}_w)$, in Figures 1d–1f, respectively. Figure 1 also shows the results of MVA after a bandpass filter over the frequency range of 0.1–2 Hz is applied to the synthetic time series data. The wave ellipticity obtained from MVA (ε_{MVA}) is shown in Figure 1g, where −1 indicates left-handed polarization and +1 right-handed polarization, and Figure 1h displays the MVA-derived wave
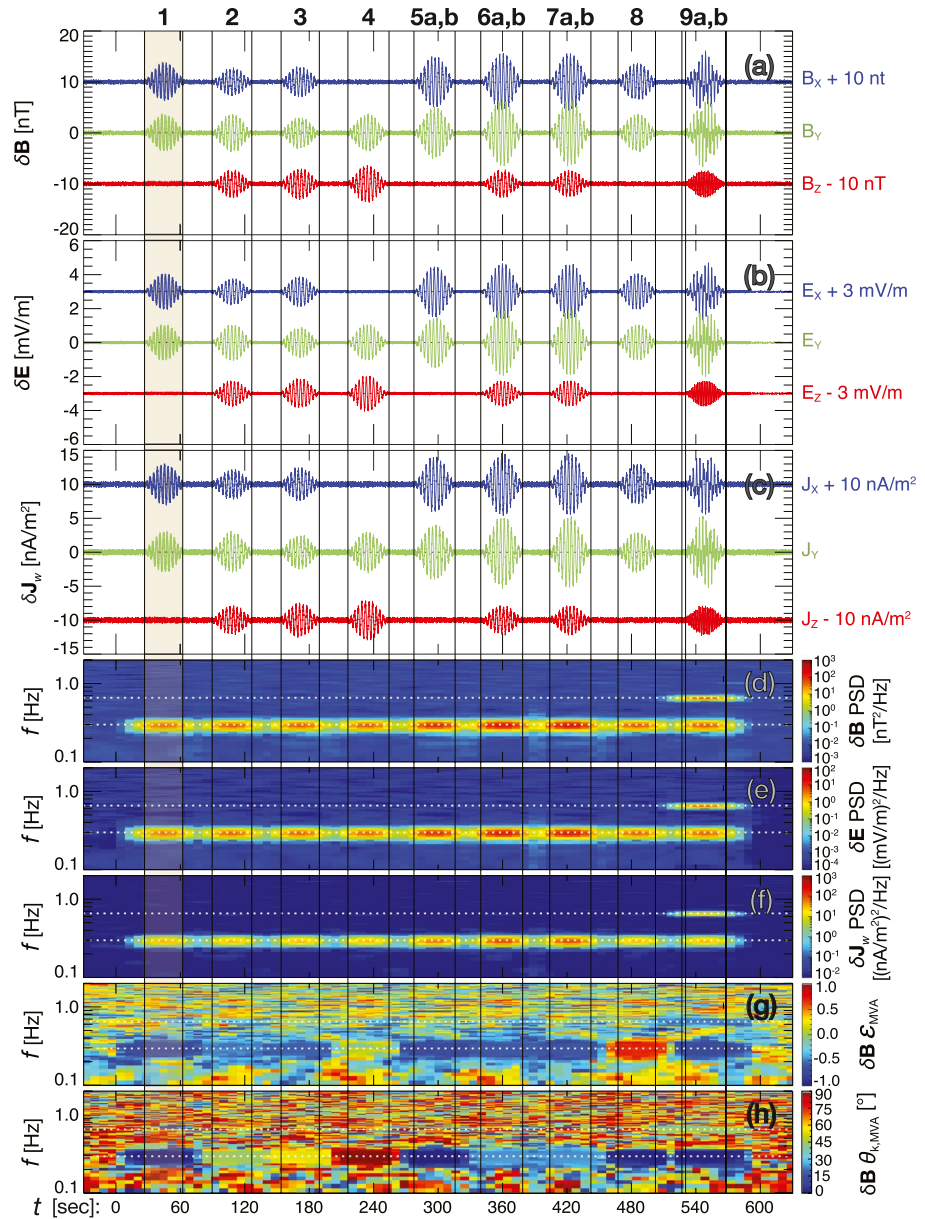
Figure 1. Synthetic EMIC wave packets constructed using varying wave vector components and ellipticities. (a) The magnetic field, $\delta\mathbf{B}$, (b) electric field, $\delta\mathbf{E}$, and (c) associated current density, $\delta\mathbf{J}_w$, waveforms of the resulting waves are shown with their corresponding (d–f) wave power spectral densities [PSD, denoted in text as $P_f(\delta\mathbf{B})$, $P_f(\delta\mathbf{E})$, and $P_f(\delta\mathbf{J}_w)$], along with (g) the wave ellipticity, $\varepsilon_{\mathrm{MVA}}$, where -1 (+1) denotes left-handed (right-handed) polarization, and (h) wave normal angle, $\theta_{k,\mathrm{MVA}}$, determined from applying MVA to the synthetic wave magnetic field. The X (blue traces) and Z (red traces) components of the $\delta\mathbf{B}$, $\delta\mathbf{E}$, and $\delta\mathbf{J}_w$ waveforms are shown with constant offsets of 10 nT, 3 mV/m, and 10 nA/m², respectively, while the Y components (green traces) remain unshifted. Vertical lines mark the time intervals used for calculation of $\mathbf{k}$ via the wave curl technique. Wave packet intervals marked 5, 6, 7, and 9 are composed of two individual waves that overlap in time. White, dashed horizontal lines in panels (d–h) denote the frequencies used to generate the synthetic wave packets at $f = 0.3$ Hz for packets 1–9a and $f = 0.66$ Hz for packet 9b. See Table 1 for more details of the individual input wave parameters.

normal angle ($\theta_{k,\mathrm{MVA}}$) (see Means, 1972; Samson & Olson, 1980). The wave ellipticities and normal angles from MVA agree very well with the input wave parameters for the single wave packets, as expected. Synthetic wave packet 4, which is not a superimposed packet, appears to be linearly polarized in Figure 1g. That is due to $\varepsilon_{\mathrm{MVA}}$ being determined from the projection of the wave oscillations onto the plane perpendicular to the background magnetic field rather than the plane perpendicular to $\mathbf{k}$.
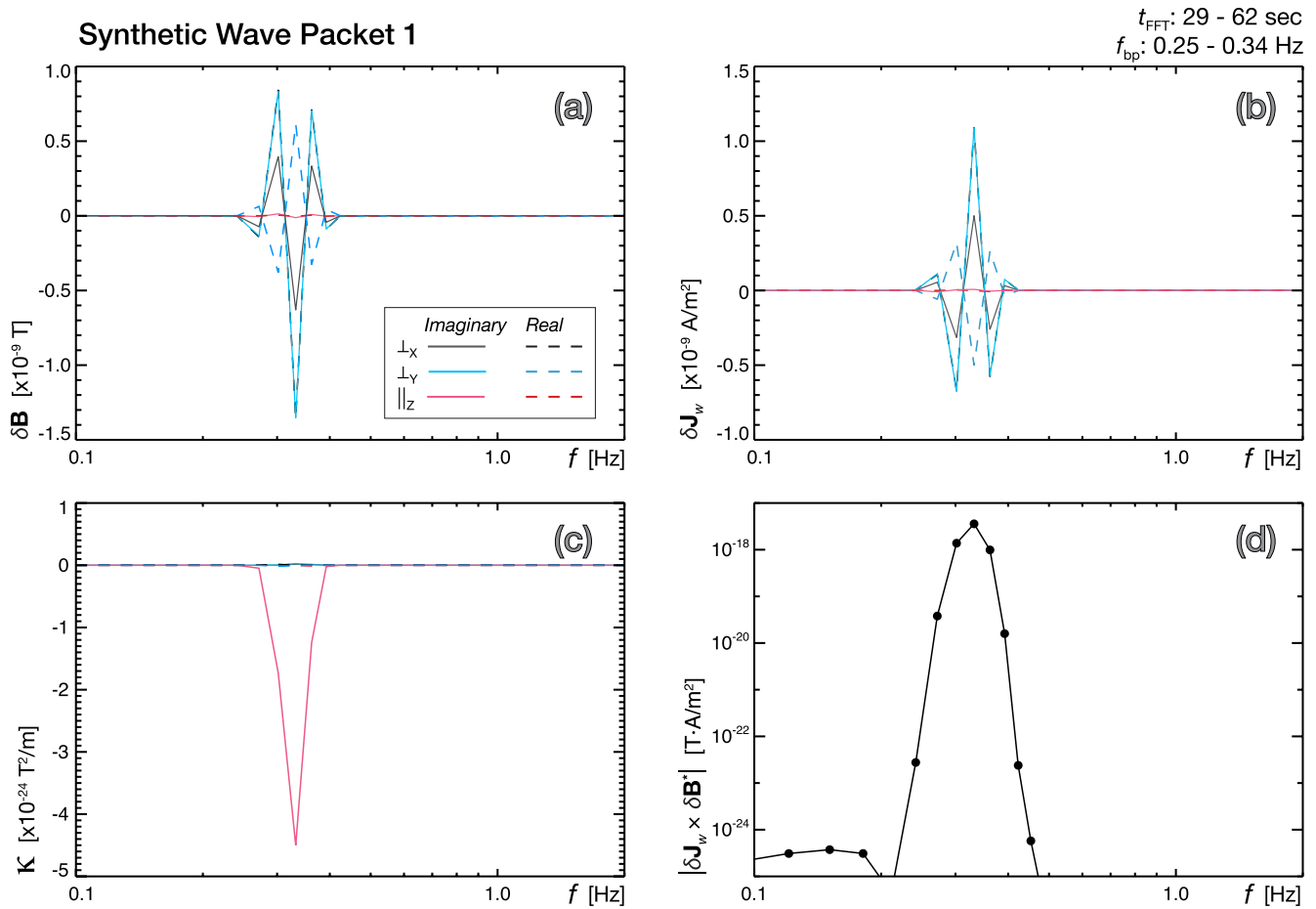
Figure 2. Application of the wave curl analysis to an idealized EMIC wave (synthetic wave packet 1, shaded region in Figure 1). FFTs of (a) $\delta\mathbf{B}_{s1}$ and (b) $\delta\mathbf{J}_{s1}$ showing the real (dashed lines) and imaginary (solid lines) components as a function of frequency. The next step of the analysis produces the (c) resulting vector, $\boldsymbol{\kappa}$ ($\boldsymbol{\kappa} \equiv \mu_0 \delta\mathbf{J}_w \times \delta\mathbf{B}_w^* = -i \, |\delta\mathbf{B}_w|^2 \, \mathbf{k}$), and the final weighting of $\mathbf{k}$ arises from (d) the magnitude of $\delta\mathbf{J}_{s1} \times \delta\mathbf{B}_{s1}^*$.

Figure 2 illustrates the implementation of the wave curl analysis to determine $\mathbf{k}$ for synthetic wave 1 (denoted as "s1"). The complex spectral components of $\delta\mathbf{B}_{s1}$ as a function of frequency are shown in Figure 2a, and the complex spectral components of $\delta\mathbf{J}_{s1}$ are shown in Figure 2b. To generate the complex spectral components of $\delta\mathbf{B}_{s1}$ and $\delta\mathbf{J}_{s1}$ in Figures 2a and 2b, respectively, a bandpass filter of 0.25–0.34 Hz, corresponding to the peak wave power seen in the dynamic power spectra of Figures 1d–1f, was first applied to the $\delta\mathbf{B}_w$ and $\delta\mathbf{J}_w$ time series shown in Figure 1. Then an FFT was applied using a time window of 32 s centered on synthetic wave packet 1 ($t_{FFT} = 29–62$ s). It should be noted that care must be taken when applying narrow bandpass filters: applying too narrow of a frequency range can lead to a reduction of the wave amplitude and introduction of artificial phase shifts due to roll-off of the filtering function at the edges of the pass band. The frequency range of the bandpass filter used for the analysis of synthetic wave 1 is not seen to introduce such an effect on the waveform, although application of a smaller frequency range for the filtering does (not shown).

The complex vector $\boldsymbol{\kappa} = \mu_0 \delta\mathbf{J}_{s1} \times \delta\mathbf{B}_{s1}^*$ (i.e., the numerator of Equation 6, where the Fourier transform of $\delta\mathbf{B}_{s1}$ and the Fourier transform of $\delta\mathbf{J}_{s1}$ are used to evaluate the cross product) is displayed in Figure 2c. This quantity more clearly shows the contribution to $\mathbf{k}$ from individual components of the resulting cross product as a function of frequency (especially when computing the weighted average of $\mathbf{k}$ using Equation 7). Following from Equation 6, $\boldsymbol{\kappa}$ is expected to have the largest contributions from the imaginary part of the vector for nonevanescent waves; the largest component of $\boldsymbol{\kappa}$ in Figure 2c is the imaginary $\kappa_{||}$ component (solid red line in Figure 2c), which is sharply peaked near $f = 0.3$ Hz. The magnitude of $\delta\mathbf{J}_{s1} \times \delta\mathbf{B}_{s1}^*$ in

Figure 2d is also sharply peaked near 0.3 Hz, consistent with the input synthetic wave frequency of 0.3 Hz. From Equation 7, the calculated **k** for synthetic wave 1 is $\mathbf{k}_{av} = (-3.44 \times 10^{-7}, -7.99 \times 10^{-6}, 1.01 \times 10^{-3})$ rad/km^{-1}. This gives a wave normal angle, $\theta_{k,av} = \tan^{-1}\left(k_{\perp} / k_{\parallel}\right)$, of 0.45°, in excellent agreement with the input **k** used in Equations 8–10 to generate this wave (see Table 1). From MVA, the wave ellipticity is found to be −0.71, consistent with a left-handed, circularly polarized wave, and the frequency of the peak $\delta\mathbf{B}_w$ power is 0.32 Hz, agreeing well with the frequency used to generate synthetic wave 1.

Table 1 shows the results of the wave curl analysis applied to all of the synthetic wave packets shown in Figure 1. The wave curl analysis implementation is seen to successfully determine **k** for all of the single, monochromatic wave packets, including the two waves at different frequencies of packet 9. However, as expected and discussed in Anderson et al. (1996), Denton et al. (1996), and Min et al. (2017), applying MVA and the wave curl analysis to synthetic waves 6 and 7, both composed of superposed packets, results in **k** and θ_k resembling neither of the constituent packets. Instead, the calculated $\mathbf{k}_{av}$ appears to be an average of the two constituent packets. For both synthetic waves 5 and 7 as compared to synthetic waves 1 and 6, respectively, the phase difference between the superposed packets comprising waves 5 and 7 does not appear to have an effect on the resulting **k** determined by Equations 6 and 7, but this could possibly impact determinations of **k** using other observational techniques like the phase differencing method (J. H. Lee et al., 2019). How the effects of wave superposition manifest in the wave curl **k** determination for packets that are only slightly overlapping in time remains to be seen in future, more in-depth analysis. While issues related to superposition of wave packets remain, these results demonstrate that this implementation of determining **k** is valid and accurate for waves composed of a single, predominant **k**, as well as for determining **k** for multiple wave bands if appropriate frequency filtering is utilized to isolate the wave of interest.

4. Application to an EMIC Wave Observation

4.1. MMS Data and EMIC Wave Example

While the primary science goal of MMS is to understand the physics of magnetic reconnection (Burch et al., 2016), the configuration and orbit of the MMS spacecraft (Fuselier et al., 2016) also make the mission ideally suited to study EMIC wave properties. The MMS mission consists of four identical spacecraft flying in a tetrahedral configuration making highly precise magnetic field, electric field, and plasma observations (Burch et al., 2016). Wang et al. (2017) have demonstrated the usefulness of MMS for a statistical study of EMIC waves, although they limited their study to polarization analysis from single-spacecraft MVA techniques. Along with determining the general characteristics of EMIC waves in the magnetosphere as demonstrated by Wang et al. (2017), differences in the wave fields between the four MMS spacecraft can be used to derive the three-dimensional gradients in the wave fields. The close spacing of the MMS spacecraft and in-flight magnetometer inter-calibration (to within ~100 pT), allow precise evaluation of the three-dimensional gradients in the magnetic field (Russell et al., 2016; Zhao et al., 2016). For example, the current density, calculated from $\nabla \times B = \mu_0 \mathbf{J}$ (via the curlometer technique [Dunlop et al., 1988]), is part of routine MMS data analysis enabled by the constellation configuration of MMS (e.g., Torbert et al., 2016).

Figures 3 and 4 show an EMIC wave observation from MMS on 2015-10-28 at 15:42 to 15:45 UT. Magnetic field data from the FGM instrument (Russell et al., 2016) on all four spacecraft are used to obtain the current density using the curlometer technique at the barycenter of the MMS constellation (see Figure 3b). The magnetic field measurements are shifted to a common reference time when applying the curlometer technique, but no time shifts are applied to the waveforms from the individual spacecraft plotted together in Figure 4 (left column). Additionally, electric field waveforms from the electric field double probe (EDP) data set (Torbert et al., 2016), which combines measurements from the Spin-plane Double Probes (Lindqvist et al., 2016) and the Axial Double Probes (Ergun et al., 2016), are shown for each spacecraft in the right column of Figure 4. This analysis uses the fast-survey mode data products, where FGM samples the magnetic field at 16 vec/s and EDP provides the electric field at 32 vec/s (see Torbert et al. (2016) for more details on MMS measurement modes).

At the time of this EMIC wave observation, MMS was located near the magnetopause at a radial distance of 10.4 R$_E$, at 15:00 magnetic local time, and at −22.7° magnetic latitude. This wave packet is a part of a
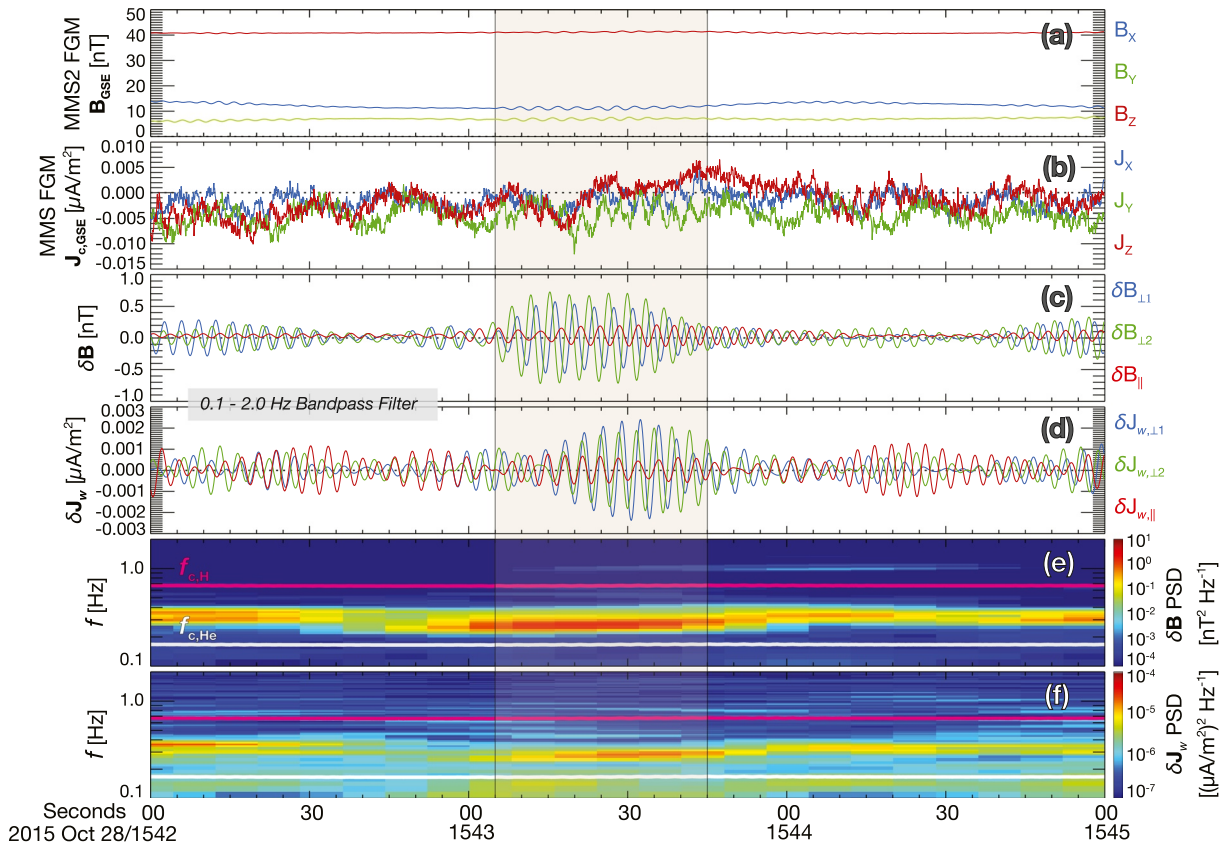
Figure 3. MMS observations of an EMIC wave on 2015-10-28 from 15:42 to 15:45 UT. (a) The magnetic field is from MMS2 FGM observations (in GSE coordinates, $\mathbf{B}_{GSE}$), while (b) the current density (in GSE, $\mathbf{J}_{c,GSE}$) at the barycenter of the MMS tetrahedron is derived from the curlometer technique using FGM data from all four spacecraft. (c and d) The MMS2 $\delta\mathbf{B}$ and barycenter $\delta\mathbf{J}_w$ wave forms are shown in magnetic field-aligned coordinates, with (e) and (f) the corresponding $\delta\mathbf{B}$ and $\delta\mathbf{J}_w$ power spectral densities. The magenta and gray traces in (e) and (f) mark the local proton and helium gyrofrequencies, respectively. The shaded region from 15:43:05 to 15:43:45 UT marks the time interval of the EMIC wave used in the wave curl analysis.

several-hours-long EMIC wave observation described in Vines et al. (2019). Figure 3 displays observations of the background magnetic field ($\mathbf{B}_{GSE}$, Figure 3a), magnetic field waveform ($\delta\mathbf{B}$, Figure 3c), and magnetic wave power ($P_f(\delta\mathbf{B})$, Figure 3e) from MMS2. The current density at the barycenter of the tetrahedron derived from the curlometer technique, $\mathbf{J}_{c,GSE}$, and wave-associated current density, $\delta\mathbf{J}_w$, is shown in Figures 3b and 3d, respectively, along with the corresponding power spectral density, $P_f(\delta\mathbf{J}_w)$, in Figure 3e. For both the background magnetic field and current density, a bandpass filter of 0.1–2.0 Hz is first applied to produce the wave fields in Figures 3d and 3e. The wave fields are then rotated from GSE coordinates into magnetic field-aligned coordinates, with $\hat{\mathbf{e}}_{\parallel} = \hat{\mathbf{b}} = \mathbf{B}/|\mathbf{B}|$, $\hat{\mathbf{e}}_{\perp 1} = \hat{\mathbf{e}}_{\perp 2} \times \hat{\mathbf{b}}$ (approximately radially outwards), and $\hat{\mathbf{e}}_{\perp 2} = \hat{\mathbf{b}} \times \mathbf{r}_{sc}/|\mathbf{r}_{sc}|$, where $\mathbf{r}_{sc}$ is the spacecraft position vector. The same bandpass filter and rotation into magnetic field-aligned coordinates was applied to the background magnetic and electric field measurements from all four spacecraft to produce the waveforms in Figure 4.

Important for using multi-point measurements for determining wave properties, the observations from the four MMS spacecraft are exceptionally similar for this event, particularly in the magnetic field observations (Figure 4, left column). Slight differences in the electric field waveforms between the spacecraft (Figure 4, right column) is likely due to the higher time cadence of EDP and possibly other noise sources in the electric field measurements. The measurements from the individual spacecraft are clearly of the same EMIC wave packet, with no indication of spatial aliasing or significant spatiotemporal evolution of the wave packet between the spacecraft locations. While the magnetic field observations from each of the MMS spacecraft overplotted together in Figure 4 are nearly identical, enough difference between the magnetic
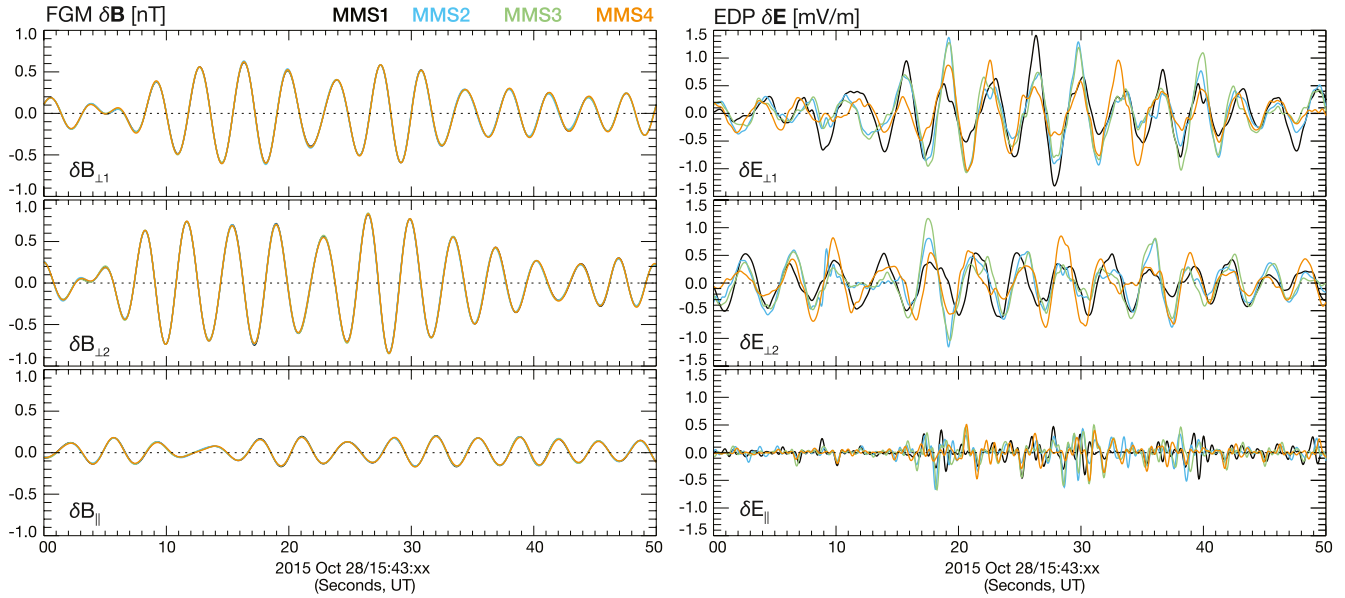
Figure 4. EMIC wave observation from all four MMS spacecraft from 15:43:00 to 15:43:50 UT on 2015-10-28. Magnetic field (left) and electric field (right) waveforms in magnetic field-aligned coordinates from all four spacecraft (MMS1 in black, MMS2 in blue, MMS3 in green, and MMS4 in orange), showing the similarity of the waveforms in all components across the four spacecraft.

field waveforms remains to allow for the determination of $\delta\mathbf{J}_w$ at the barycenter of the tetrahedron (i.e., the coherency of the wave between individual MMS observations is greater than 95%, not shown).

Focusing on the packet between 15:43:05 and 15:43:45 UT (highlighted by the yellow box in Figure 3), the peak emission ($P_f(\delta\mathbf{B}) > 1.0$ nT^2/Hz and $P_f(\delta\mathbf{J}_w) > 10^{-5}$ (μA/m^2)^2/Hz) occurs at frequencies between ~0.27 and 0.30 Hz (Figures 3e and 3f), falling between the local proton and helium gyrofrequencies (magenta line and gray line, respectively, in Figures 3e and 3f). From MVA (shown in Vines et al., 2019), this EMIC wave is observed to be left-handed, circularly polarized, with a small wave normal angle and a Poynting vector directed parallel to the background magnetic field. These signatures are typical of proton-band EMIC waves propagating along the background magnetic field (e.g., Mauk & McPherron, 1980; Rauch & Roux, 1982; Stix, 1992).

For applying the wave curl technique to this packet, we obtain single-sided power spectra from FFTs with a Hanning window over the time interval of 15:43:05–15:43:45 UT of the $\delta\mathbf{B}$ and $\delta\mathbf{J}_w$ waveforms at the barycenter of the MMS tetrahedron. Before applying the FFTs, the magnetic field and current density time series data is more finely filtered using a bandpass filter for the frequencies of 0.221–0.391 Hz and rotated into a magnetic field-aligned coordinate system. As noted in Section 3 when applying the wave curl analysis to the synthetic waveforms, care must be taken when using narrow filtering functions in order to avoid introducing artificial signals in the waveforms. For this EMIC wave packet, the bandpass filter frequency range used in the analysis does not appear to introduce these adverse effects (not shown). The components of the resulting complex spectral wave fields (shown in Figures 5a and 5b for the Fourier transforms of $\delta\mathbf{B}$ and $\delta\mathbf{J}_w$, respectively) are then used in Equation 6 to obtain the components of $\mathbf{k}$ at the barycenter of the constellation. As done in Figure 2, the vector $\boldsymbol{\kappa}$ is shown in Figure 5c, along with the magnitude of the $\delta\mathbf{J}_w \times \delta\mathbf{B}^*$ term from Equation 6 in Figure 5d. The components of $\boldsymbol{\kappa}$ derived using data from MMS in Figure 5c appear remarkably similar to the synthetic wave packet results in Figure 2c, with the imaginary $\kappa_{||}$ component having the largest value. However, there are also contributions from the perpendicular components for the observed wave packet (blue and black solid lines in Figure 5c). Taking the weighted average of $\mathbf{k}$ (Equation 7) results in a highly magnetic field-aligned wave vector: $\mathbf{k} = [k_{\perp,1}, k_{\perp,2}, k_{||}] = [-3.47 \times 10^{-4}, 2.14 \times 10^{-4}, 3.30 \times 10^{-3}]$ rad/km, which gives a wave normal angle of 7.1°. This wave vector corresponds to a wavelength $\lambda = 2\pi/k = 1891.6$ km, and a peak frequency, $f_{\text{peak}} = 0.276$ Hz ($\omega = 1.736$ rad/s), determined by the frequency where $P_f(\delta\mathbf{B})$ maximizes.
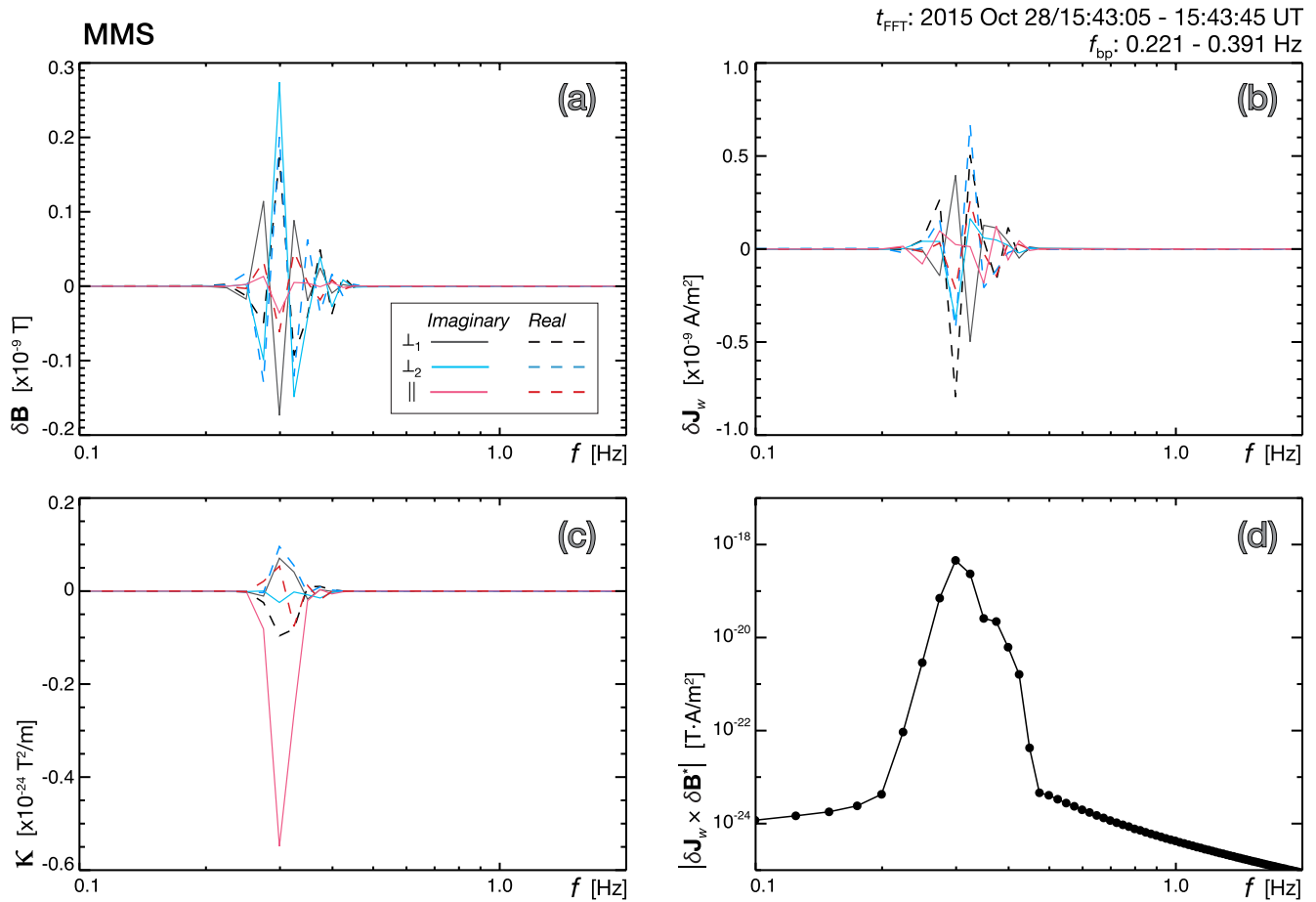
Figure 5. Application of the wave curl analysis to the observed EMIC wave on 2015-10-28 from 15:43:05 to 15:43:45 UT (highlighted in Figure 3), using a band-pass filter of 0.221–0.391 Hz, in the same format as Figure 2, with the $\perp_1$ component in black, $\perp_2$ component in blue, and $\parallel$ component in red for panels (a)–(c). $\delta\mathbf{B}$ and $\delta\mathbf{J}_w$ are from the barycenter of the MMS constellation.

4.2. Sensitivity to Time and Frequency Selection

To investigate the sensitivity of the wave curl method to the initial selection of frequency and time intervals required for the FFT, the analysis was performed for different combinations of bandpass frequency ranges (Δf) and time intervals (Δt). Shown in Figure 6, the longest time interval was selected to fully encompass the EMIC wave packet. From this interval, the center time of the wave packet, t_0, was set at 15:43:25 UT. The time intervals for analysis were then systematically increased from $\Delta t = t_0 \pm 4.0$ s (15:43:21–15:43:29 UT, the center 10% of the largest time interval) to $\Delta t = t_0 \pm 20$ s (15:43:05–15:43:45 UT, the longest time interval, also marked by the shaded area in Figure 3) in evenly spaced steps of ± 1.6 s for each successive window. Additionally, the frequency range of the bandpass filter applied to the background magnetic field was systematically increased from a very narrow frequency range of $\Delta f = 0.241$–0.326 Hz (encompassing the frequency of the peak power in $\delta\mathbf{B}$) up to a broader range of $\Delta f = 0.1$–2.0 Hz (horizontal dotted lines in Figure 6b). The coarsest frequency range used in this sensitivity assessment was chosen to be a broad window well beyond the frequencies of the $P_f(\delta\mathbf{B})$ enhancement seen for this wave packet (Figures 3e and 6b), while the finest frequency range was chosen to capture a very narrow portion of the $P_f(\delta\mathbf{B})$ enhancement. Logarithmically evenly spaced frequencies between the lower frequency of the narrowest window to the lower frequency of the coarsest window define the lower bound of the increasingly coarse frequency ranges. Similarly, logarithmically evenly spaced frequencies between the upper frequency of the narrowest window and the upper range of the coarsest window define the upper bounds. The exact Δf and Δt ranges are listed in Figure 7.

The wave curl analysis was applied using each combination of time and frequency range, with the resulting wave normal angles shown in Figure 7. The greatest variation in the wave normal angle arises from
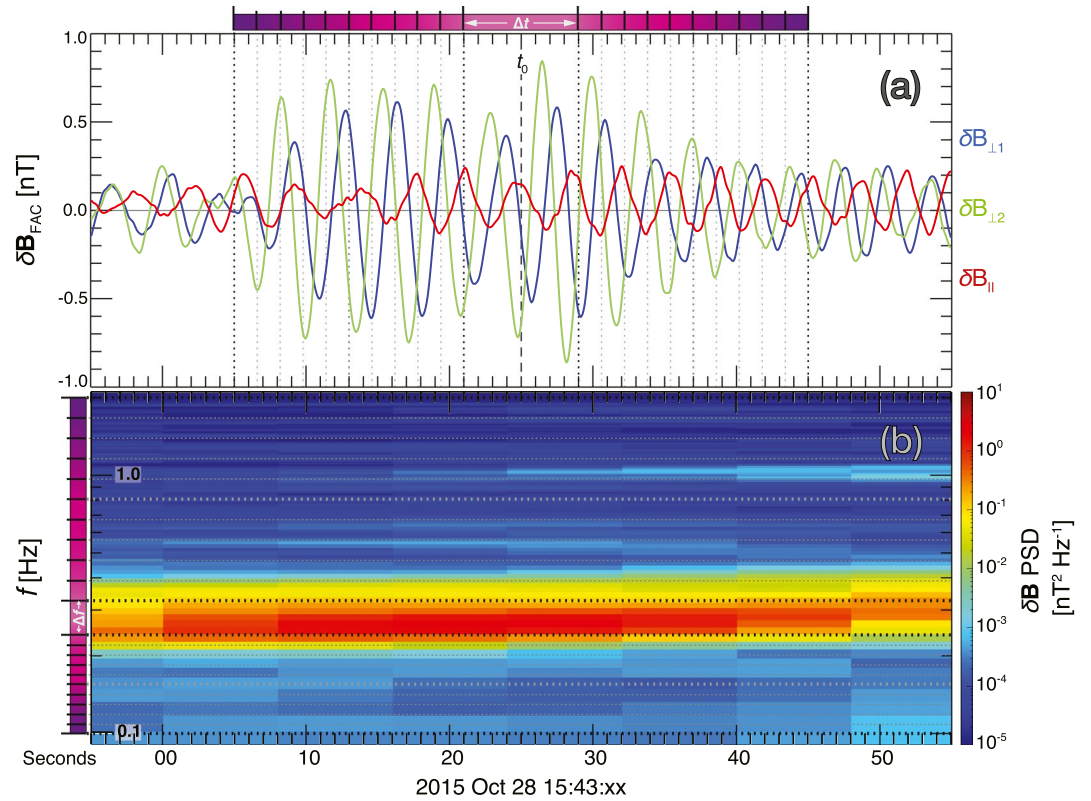
Figure 6. (a) $\delta\mathbf{B}$ waveform and (b) power spectral density of the EMIC wave observation from MMS. The vertical dotted lines show the duration of the time intervals used for the FFTs of $\delta\mathbf{B}$ and $\delta\mathbf{J}_w$, increasing in duration from the center of the window by ±1.6 s for each successive time interval. The horizontal lines in (b) show the frequency width of the bandpass filters used for the FFTs, becoming increasingly coarser from the initial narrow filtering around the peak in $\delta\mathbf{B}$ power. The time intervals (Δt) and frequency ranges (Δf) used for the technique sensitivity assessment are also denoted by the colored bars above panel (a) and to the left of panel (b), respectively. These ranges are listed in Figure 7, with details on the determination of the ranges in the text.

use of very short time windows (bottom region of Figure 7), where only 2–4 wave periods comprise the FFT (Figure 6a), along with broad frequency ranges for the bandpass filter (right-side of Figure 7), where emission unrelated to the wave packet of interest may be present (e.g., the narrow-band feature around 1.0 Hz in Figure 6b). Additionally, using the narrowest frequency range when applying a bandpass filter to the waveforms results in reduction of the wave amplitude by ∼10%–15% as compared to the pass band highlighted by the magenta box in Figure 7 and used to evaluate **k** for this wave packet in Section 4.1 (not shown). Overall, though, the wave normal angle does not vary greatly over the different ranges of time and frequency selections, with θ_k values ranging from 1.0° to 12°. The consistency with the time window length indicates that the time-coherence for this packet is high, that is there are no strong phase skips (see e.g., Engebretson et al., 2018), consistent with a low-degree of wave superposition. This also suggests that the wave curl technique is not highly sensitive to the selection of appropriate bandpass filter and time ranges, as long as the time window includes more than ∼3 wave periods and the frequency bandpass filter does not include other strong emissions (e.g., broadband noise and other wave packets) and is broad enough to not distort the waveform due to roll-off of the filtering function.

4.3. Comparison With Theoretical Linear Dispersion Relation

Using the local background plasma and magnetic field conditions observed from 2015-10-28/15:42 to 15:44 UT, the theoretical wave dispersion relation for the observed wave packet was determined using the Waves in Homogenous, Anisotropic, Multi-component Plasma (WHAMP) dispersion relation solver (Ronnmark, 1982). For this wave packet interval, six ion populations are included with the thermal electron
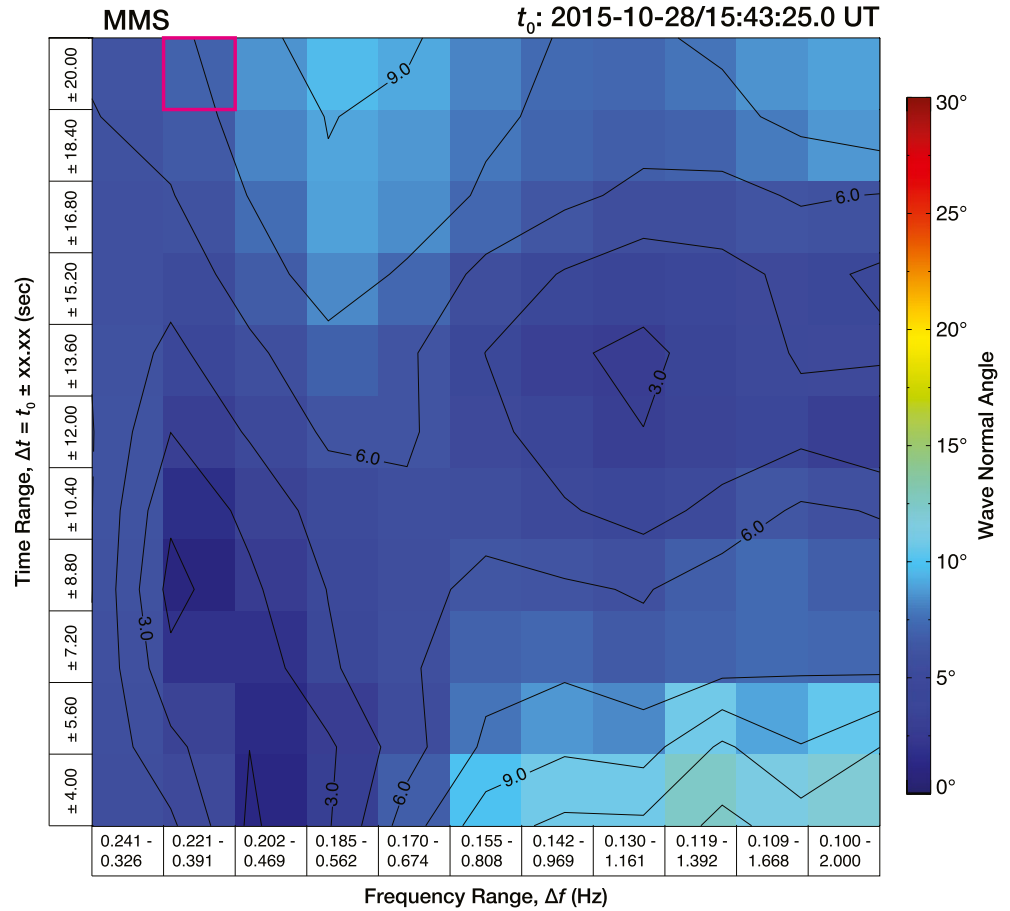
Figure 7. The calculated wave normal angle (color) as a function of the frequency range (Δf) and time interval (Δt) used for the FFTs of $\delta \mathbf{B}$ and $\delta \mathbf{J}_w$, showing how varying the time interval duration and bandpass frequency width affects the resulting $\mathbf{k}$ components after applying the wave curl analysis. The frequency and time window used for the wave curl results and comparisons with the dispersion relation and other techniques is marked by the magenta square.

population: a "hot" and "cold" component for H^+, He^+, and O^+. Density and temperature moments used in the WHAMP dispersion relation solver are taken from MMS Hot Plasma Composition Analyzer (HPCA) (Young et al., 2016) observations of H^+, He^+, and O^+, where the hot population is comprised of ions with energies of 1–40 keV, and the cold population consisting of ions with energies of 1 eV–1 keV. This time interval is particularly fortuitous, as nearly the entirety of the low-energy ion distribution appears to be present in the MMS observations: the total of each ion species density measured by HPCA and the density derived from the electron plasma frequency are in very good agreement for this event (see Figure 3 of Vines et al. [2019]). The electron perpendicular temperature is chosen to be 5 eV (~10 times lower than the cold H^+ temperature), and no parallel drift velocity is included for any of the plasma populations. As discussed in Vines et al. (2019), this wave packet is expected to be near the wave generation region in the outer dayside magnetosphere during this time on 2015-10-28. For this reason, the observed $\mathbf{k}$ should ideally be very similar to $\mathbf{k}$ derived from the dispersion relation given the observed local plasma conditions. Figure 8a shows the resulting dispersion surface from WHAMP, where the color shows the normalized wave growth rate, γ/Ω_{cp} (where $\Omega_{cp} = eB/m_h$ is the proton gyrofrequency), with red (blue) indicating wave growth (damping). The components of $\mathbf{k}$ are normalized by the hot proton parallel gyroradius, $\rho_{||}$, which for this interval is 191.53 km for protons with energies above 1 keV. Consistent with prior observations, this interval is unstable to EMIC wave growth in the proton band over a fairly wide swath of $\mathbf{k}$ values for normalized frequencies between ω/Ω_{cp} of ~0.3–0.45. Interestingly, wave growth is shown to be possible for somewhat larger $k_\perp$ (with θ_k reaching up to ~30°) during this time interval.
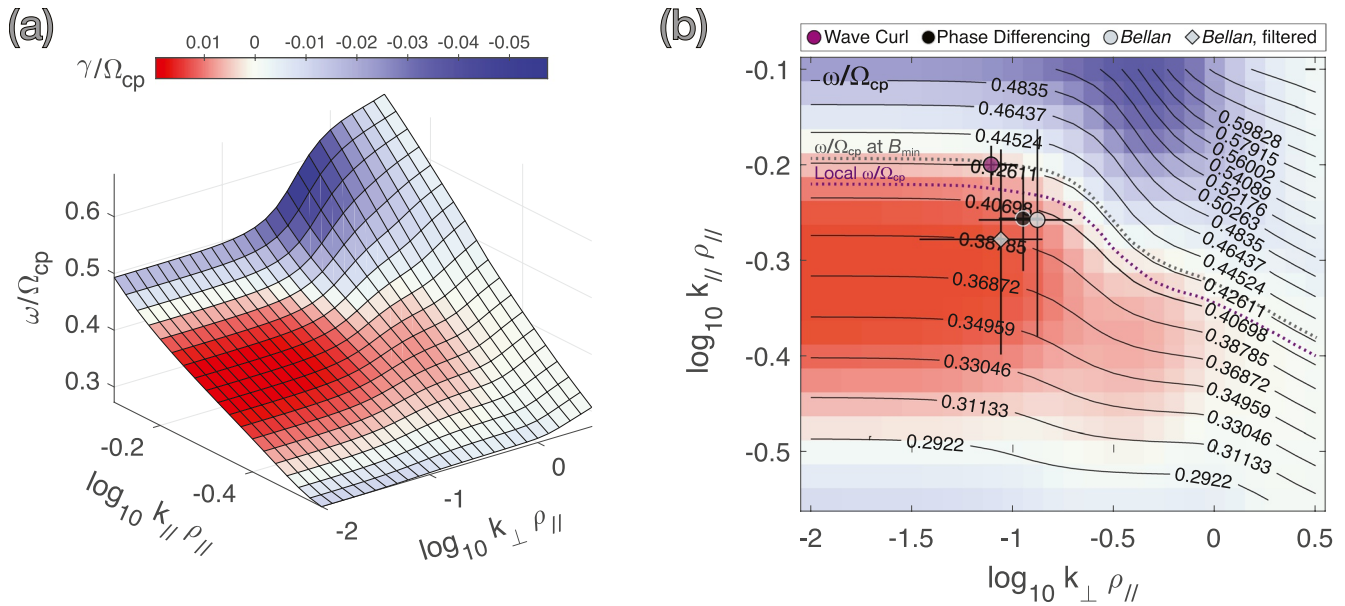
Figure 8. (a) WHAMP dispersion surface showing normalized wave growth (γ/Ω_{cp}) as a function of the normalized wave frequency (ω/Ω_{cp}) and normalized **k** components ($k_\parallel \rho_\parallel$, $k_\perp \rho_\parallel$). Ion moments of H^+, He^+, and O^+ with energies of 1–40 keV measured by HPCA on MMS2 from 15:42 to 15:44 UT were used as inputs for WHAMP. (b) Two-dimensional projection of the WHAMP dispersion surface with black contours showing ω/Ω_{cp} and colors showing γ/Ω_{cp}. The filled symbols show the calculated **k** components from applying three different methods to the EMIC wave at 15:43:05–15:43:45 UT: wave curl analysis (purple), phase differencing (black), and the Bellan (2016) method with (gray diamond) and without (gray circle) bandpass filtering applied to the observations. The derivation of the error bars for each method are described in the text. The purple dashed line marks the observed normalized frequency for the MMS observation, and the gray dashed line shows the normalized frequency when using the proton gyrofrequency at the local minimum in **B** region ($f_{cp,min} = 0.965 f_{cp,local}$) where the wave was likely generated.

The normalized **k** components from the WHAMP dispersion surface are shown again in Figure 8b using the same color scale for the normalized wave growth rate, but with the normalized frequencies from the dispersion surface now shown as overlaid contours. As a comparison with the observed wave properties, the purple circle marks the normalized **k** components derived for this wave packet from the wave curl technique described earlier, and listed in Table 2. The error bars illustrate the variation in **k** from the wave curl analysis due to time and frequency range selection, and are determined by the standard deviation of all resulting **k** values shown in Figure 7 ($\sigma_{k,\parallel} = 1.55 \times 10^{-4}$ rad/km and $\sigma_{k,\perp} = 1.43 \times 10^{-4}$ rad/km). This is likely a conservative error estimate, since the values include intervals using the small-time-window, large-frequency-window values (bottom right bins in Figure 7), which produce outliers in the sample of calculated **k** components. For this wave packet, the observed frequency corresponding to the maximum $P_f(\delta \mathbf{B})$, $\omega = 1.736$ rad/s, is normalized to the local Ω_{cp} (from conditions used in the WHAMP solver, $\Omega_{cp} = 4.183$ rad/s) and shown by

Table 2
*Comparison of Observational Methods to Estimate **k***

Method	Frequency [Hz]	ω/Ω_{cp}	$k_\parallel$	$k_{\perp 1}$	$k_{\perp 2}$	$\lvert k \rvert$	θ_k [°]
			k [$\times 10^{-3}$ rad/km]	
Wave curl[a]	0.276	0.415	3.30	−0.347	0.214	3.32	7.1
		(0.429 at B_{min})					
Phase differencing	0.309 (Average)	0.464	2.90	0.581	−0.0916	2.96	11.5
Bellan (2016)[a]	0.275	0.413	2.89	−0.590	0.359	2.97	13.5
Bellan (2016)[a], with filtering	0.275	0.413	2.75	−0.386	0.243	2.79	9.4
MVAB for MMS2	0.276	0.415	–	–	–	–	16.1
MVAE for MMS2	0.276	0.415	–	–	–	–	11.4

[a]Current density and magnetic field data at the barycenter of the MMS constellation.

the purple dotted line ($\omega/\Omega_{cp} = 0.415$). To determine how much the normalized frequency of the wave may vary from the possible generation region, ω/Ω_{cp} is also calculated for the modeled magnetic field minimum magnitude (B_{min}) via $\Omega_{cp,min} = (B_{min}/|\mathbf{B}|)\omega$. B_{min} is obtained from the T01 magnetic field model (Tsyganenko, 2002a, 2002b) using upstream solar wind conditions from the OMNI data set (King & Papitashvili, 1994; https://omniweb.gsfc.nasa.gov) for 2015-10-28/15:42 UT. The normalized frequency at the modeled B_{min} ($\omega/\Omega_{cp,min} = 0.429$) is shown by the gray dotted line. For this interval, the Doppler-shifted wave frequency is determined from the average ion velocity from the MMS2 Fast Plasma Investigation – Dual Ion Spectrometer (FPI-DIS) (Pollock et al., 2016) fast survey observations between 2015-10-28/15:42:55 and 15:43:55 UT and the $\mathbf{k}$ vector from the wave curl method ($\omega_{wave} = 2\pi f_{wave} = 2\pi f_{obs} - \mathbf{k} \cdot \mathbf{v}_i$). This results in a normalized frequency of $\omega_{wave}/\Omega_{cp} = 0.410$ (with a minimum and maximum of 0.402 and 0.418, respectively, using instantaneous $\mathbf{v}_i$ values), very similar to the observed normalized frequency marked in Figure 8b. Although not coincident with the maximum wave growth, the $\mathbf{k}$ components and normalized observed frequency of the wave packet agree remarkably well with the dispersion relation, and are seen to correspond to a region of possible wave growth.

While the real frequency based on the dispersion relation using the wave curl estimate of $\mathbf{k}$ is in excellent agreement with that of the observed wave using B_{min} (comparing the purple circle and dashed gray curve in Figure 8b), and the growth rate based on the dispersion relation is positive (purple circle within the red region of Figure 8b), the region of maximum growth rate (darkest red color in Figure 8b) is at lower values of $k_{\parallel}$ than those of the wave curl $\mathbf{k}$. Noting that this particular wave packet is outside of the likely wave generation region, the lower value of the growth rate for the observed $\mathbf{k}$, in combination with the observed normalized frequency being very similar to the frequency at the likely wave generation region, may point to propagation of the wave without any significant growth or damping occurring. It should also be noted that the plasma parameters used in this calculation may be slightly different than the plasma conditions that drove the waves. One simple effect of the growth of the EMIC waves is reduction of the anisotropy of the hot protons by transferring hot, perpendicular thermal energy to hot, parallel thermal energy (Denton, Anderson, et al., 1994; Gary et al., 1994). If the hot protons were more anisotropic, the $k_{\parallel}$ value of maximum growth rate would be increased. For instance, if the temperature ratio $T_{\perp,hot}/T_{\parallel,hot}$ were increased to 3 from the observed value of 1.79, and keeping the average temperature ($T_{av} = (2T_{\perp,hot} + T_{\parallel,hot})/3$) constant, the $\log_{10}(k_{\parallel}\rho_{\parallel})$ value of maximum growth rate would be increased by 1.6. This would bring the position region of maximum growth rate in Figure 8b (darkest red color) in alignment with the wave curl $k_{\parallel}$.

4.4. Comparison With Other Observational Techniques

Additionally, $\mathbf{k}$ has been computed from several other techniques: the multi-spacecraft phase differencing method (see Balikhin et al., 2003; J. H. Lee et al., 2019; Pinçon & Glassmeier, 2008; Turner et al., 2017), directly from the method outlined in Bellan (2016) (see supporting information of Bellan [2016]) using current density obtained from the curlometer technique and the magnetic field at the barycenter of the MMS formation, and single-spacecraft MVA (see Means, 1972; Russell et al., 2016). The resulting $\mathbf{k}$ values from the phase differencing and Bellan (2016) methods using the time interval of 15:43:05–15:43:45 UT are shown by the black and gray symbols, respectively, in Figure 8b. The results from the Bellan (2016) method are obtained using measurements with and without a bandpass frequency filter (shown in Figure 8b by the gray diamond and gray circle, respectively), where the same range of time windows and frequencies used for the wave curl results (see Figure 6) are applied to the data. In Figure 8b, the data point showing the Bellan (2016) with frequency filtering also applied is a result of using the same frequency range as that shown for the wave curl analysis, 0.221–0.391 Hz. As also done for the wave curl analysis, the characteristic wave frequency for the Bellan (2016) method is determined by the maximum in $P_t(\delta\mathbf{B})$. Error bars shown for the phase differencing method are derived from the standard deviation of the mean wave vector from all valid solutions using all of the different sets of triplet pair-combinations available from the four MMS spacecraft (see Turner et al. (2017) and the supporting information in J. H. Lee et al. (2019) for more details). As done with the wave curl analysis, error bars shown for the Bellan (2016) method results are determined by the standard deviation of the $\mathbf{k}$ values from calculations with varying time and frequency windows. For using the Bellan (2016) method without applying a bandpass filter, only the time window was varied in the same fashion as done for the wave curl analysis results (see Figure 6a). To easily compare the results from the various techniques, Table 2 lists the wave normal angle obtained by each method, along with the observed

frequencies and individual **k** components in the same magnetic field-aligned coordinate system used for the wave curl analysis.

Both of these additional multi-spacecraft methods yield normalized **k** components similar to the wave curl results and with the predicted dispersion relation, although the phase differencing method results were closer to the wave curl analysis results. However, the normalized frequency for the phase differencing method has the largest difference from the results of the other methods (second and third columns from the left in Table 2). Comparing the calculated frequency from phase differencing with the theoretical frequency for calculated **k** components, there is quite a discrepancy, despite the consistency of **k** from phase differencing with results from the other methods. The wave vector derived from the Bellan (2016) method is mostly consistent with the wave curl analysis and phase differencing results, however the normalized frequency does not agree quite as well with the theoretical normalized frequency for those calculated **k** components. Additionally, there is much more variation in the resulting **k** values from the Bellan (2016) method, particularly for $k_{||}$. The use of frequency filtering in applying the Bellan (2016) method does not as clearly help improve the results for this observation, as the values obtained with and without bandpass filtering are seen to be in family with the other methods with similar levels of variation in the resulting **k** values. The larger degree of variation from the Bellan (2016) method may arise from the use of time-averaged cross-correlations of the vector quantities prior to the Fourier transforms, as this may be introducing additional artifacts through amplifying noise in the measurements rather than just the signal of interest.

Using single-spacecraft MVA of MMS2 magnetic field observations (MVAB), the wave normal angle for this packet ranges from 3.5° to 38.2° over the frequency range of interest (0.22–0.39 Hz), with an average value of 16.1° and a median value of 14.4°. The mean value from MVAB, listed in Table 2, agrees well with the resulting wave normal angle from the wave curl technique. This is further supported by applying MVA to the electric field measurements from MMS2 (MVAE), which produces an average wave normal angle of 11.4° (with a median value of 8.42°). Applied to magnetic field observations from the other MMS spacecraft, MVAB results in nearly identical average wave normal angles of 16.6°, 16.3°, and 16.1°, for MMS1, MMS3, and MMS4, respectively. The consistency between the MVAB and MVAE results suggest that the quality of the electric field measurements during this time interval does not suffer significantly from noise sources or issues of a spacecraft wake arising from cold plasma populations, as has been observed for many spacecraft missions (e.g., André & Cully., 2012), including MMS near the magnetopause (Toledo-Redondo et al., 2019). The general agreement of the wave curl analysis implementation, the other multi-spacecraft techniques, and MVA applied to either δ**B** or δ**E** of the individual MMS spacecraft with the theoretical wave properties provide confidence of the success of the wave curl analysis technique for this particular EMIC wave observation.

5. Summary

In this paper, we have described a new method implementation, the wave curl analysis, for determining the wave vector **k** observationally through application of Ampere's law in Fourier space. The wave curl analysis takes advantage of the multi-point magnetic field measurements of the MMS spacecraft to determine the wave-associated current density used to calculate **k**. We have demonstrated the application of the wave curl analysis to both a range of synthetic wave packets and an EMIC wave event observed by MMS. EMIC waves are particularly ideal for study with MMS using this technique as the characteristic wavelengths are generally larger than the spacecraft separations, but small enough to still have slight differences observed between the individual spacecraft, and the EMIC wave emission is generally well within the frequency range allowed by the temporal sampling of the FGM instrument.

Testing the wave curl analysis on synthetic wave packets with different wave properties (specifically ellipticities and wave normal angles), the method is shown to perform remarkably well, although superposition of multiple wave packets remains a challenge in interpreting the resulting **k** properties. However, for concurrent waves in multiple bands, applying the appropriate frequency limits when filtering the data allows for the individual wave vector properties to be distinguished. When applying the wave curl analysis to an EMIC wave packet observed by MMS, the technique is shown to be fairly robust. If several wave periods are included (i.e., more than 2–3 wave periods, in this case), then the resulting wave vector does not appear to

be highly sensitive to the time interval selected. The resulting **k** values appear to have the greatest variation when using very narrow time windows with a coarse frequency range. Variation can also arise from too narrow of a bandpass frequency range, where artificial effects on the wave amplitude and phase are introduced by edge effects of the filtering function.

As shown by Vines et al. (2019), the EMIC wave packet used here for the wave curl analysis is likely very near a source region, and as such the calculated **k** is expected to agree well with the theoretical dispersion relation. Additionally, and important for properly determining the dispersion relation with WHAMP (see e.g., Denton et al. [2014]; Kozyra et al. [1984]; J. H. Lee et al. [2019]), MMS appears to have observed nearly the full plasma population for this time interval (see Vines et al., 2019), and multiple ion species with different temperatures were included in the WHAMP calculation. As shown in Figure 8b, **k** from the wave curl analysis agrees remarkably well with the normalized frequency from WHAMP for the given **k** components, and is also consistent with the wave packet being in a region of wave growth. For waves well outside of the source region, how much **k** has evolved as the waves propagate, and so how consistent with the theoretical dispersion surfaces the observed wave properties are, remains to be seen. The wave curl analysis also agrees with other single and multi-spacecraft methods, although **k** derived from the wave curl analysis is shown to agree with the dispersion relation from WHAMP somewhat better than both the phase-differencing and Bellan (2016) methods for this packet, and is shown to have less variation in the results.

In general, there are several benefits to using the wave curl analysis implemented in this study: All three individual components of **k** can be determined, no additional assumptions are made of the spacecraft position relative to the wave when using the wave fields directly, and no strict coordinate system definition is needed for proper implementation. Additionally, while **k** is determined for all frequencies allowed by the data set used, weighting $\mathbf{k}(\omega)$ by the magnitude of $\delta\mathbf{J}_w \times \delta\mathbf{B^*}$ allows for the dominant signal of interest for narrow-band, monochromatic waves to be easily identified. There are, however, certain considerations to be made for the implementation of this method. Using the magnetic field and current density does not preclude any specific wave type, but the wave curl analysis is generally limited by the fidelity of the current density measurements, particularly depending on the characteristic spatial and temporal scales of the wave mode of interest relative to the gradients in the background magnetic field, as well as the temporal sampling of the magnetic field (or possibly plasma) data used to determine the current density. Additionally, the wave curl analysis implicitly assumes the waves are plane waves, and does not disambiguate the constituents of superposed wave packets. As shown in Gershman et al. (2017), this type of analysis can be applied to a variety of wave phenomena, such as broadband kinetic Alfvén waves. However, care must be taken to understand the influence of noise or data artifacts on the wave vector results. Further work to better characterize the capabilities of the wave curl analysis includes more investigation of the effects of wave superposition, as well as application of the wave curl analysis to other wave modes.

The wave curl analysis has shown great promise in allowing systematic investigations of wave vector properties (particularly for, but not limited to, EMIC waves) measured by MMS. This will allow for an advancement in a number of long-standing problems in wave generation, propagation, evolution, and wave-particle interactions that require direct and accurate knowledge of the wave vector.

Data Availability Statement

MMS L2 data sets are available to the public through the MMS Science Data Center (https://lasp.colorado.edu/mms/sdc/public/). IDL routines for display of MMS data are also publicly available in the current SPEDAS software package, which can be found through the MMS Science Data Center and through the SPEDAS website (http://spedas.org). WHAMP codes, available for Fortran 95 and MATLAB, and documentation can be found at https://github.com/irfu/whamp.

References

Allen, R. C., Zhang, J.-C., Kistler, L. M., Spence, H. E., Lin, R.-L., Dunlop, M. W., & André, M. (2013). Multiple bidirectional EMIC waves observed by Cluster at middle magnetic latitudes in the dayside magnetosphere. *Journal of Geophysical Research: Space Physics*, *118*(10), 6266–6278. https://doi.org/10.1002/jgra.50600

Allen, R. C., Zhang, J.-C., Kistler, L. M., Spence, H. E., Lin, R.-L., Klecker, B., et al. (2015). A statistical study of EMIC waves observed by Cluster: 1. Wave properties. *Journal of Geophysical Research: Space Physics*, *120*, 5574–5592. https://doi.org/10.1002/2015JA021333

Anderson, B. J., Denton, R. E., & Fuselier, S. A. (1996). On determining polarization characteristics of ion cyclotron wave magnetic field fluctuations. *Journal of Geophysical Research*, *101*(A6), 13195–13213. https://doi.org/10.1029/96JA00633

Anderson, B. J., Erlandson, R. E., & Zanetti, L. J. (1992a). A statistical study of Pc 1–2 magnetic pulsations in the equatorial magnetosphere: 1. Equatorial occurrence distributions. *Journal of Geophysical Research*, *97*(A3), 3075–3088. https://doi.org/10.1029/91JA02706

Anderson, B. J., Erlandson, R. E., & Zanetti, L. J. (1992b). A statistical study of Pc 1–2 magnetic pulsations in the equatorial magnetosphere: 2. Wave properties. *Journal of Geophysical Research*, *97*(A3), 3089–3101. https://doi.org/10.1029/91JA02697

André, M., & Cully, C. M. (2012). Low-energy ions: A previously hidden solar system particle population. *Geophysical Research Letters*, *39*(3), L03101. https://doi.org/10.1029/2011GL050242

Balikhin, M. A., & Gedalin, M. E. (1993). *Comparative analysis of different methods for distinguishing temporal and spatial variations*. Proceedings of START Conference, Aussois, France, Vol ESA WPP 047 (pp. 183–187).

Balikhin, M. A., Pokhotelov, O. A., Walker, S. N., Amata, E., Andre, M., & Dunlop, M. (2003). Minimum variance free wave identification: Application to Cluster electric field data in the magnetosheath. *Geophysical research letters*, *30*(10), 150. https://doi.org/10.1029/2003GL016918

Bellan, P. M. (2012). Improved basis set for low frequency plasma waves. *Journal of Geophysical Research*, *117*(A12), A12219. https://doi.org/10.1029/2012JA017856

Bellan, P. M. (2016). Revised single-spacecraft method for determining wave vector **k** and resolving space-time ambiguity. *Journal of Geophysical Research: Space Physics*, *121*(9), 8589–8599. https://doi.org/10.1002/2016JA022827

Burch, J. L., Moore, T. E., Torbert, R. B., & Giles, B. L. (2016). Magnetospheric multiscale overview and science objectives. *Space Science Reviews*, *199*, 5. https://doi.org/10.1007/s11214-015-0164-9

Chen, L., Thorne, R. M., & Bortnik, J. (2011). The controlling effect of ion temperature on EMIC wave excitation and scattering. *Geophysical research letters*, *38*, L16109. https://doi.org/10.1029/2011GL048653

Chen, L., Thorne, R. M., & Horne, R. B. (2009). Simulation of EMIC wave excitation in a model magnetosphere including structured high-density plumes. *Journal of Geophysical Research*, *114*(A7), A07221. https://doi.org/10.1029/2009JA014204

Cornwall, J. M. (1965). Cyclotron instabilities and electromagnetic emission in the ultra-low frequency and very low frequency ranges. *Journal of Geophysical Research*, *70*(1), 61–69. https://doi.org/10.1029/JZ070i001p00061

Denton, R. E. (2018). Electromagnetic ion cyclotron wavefields in a realistic dipole field. *Journal of Geophysical Research: Space Physics*, *123*, 1208–1223. https://doi.org/10.1002/2017JA024886

Denton, R. E., Anderson, B. J., Gary, S. P., & Fuselier, S. A. (1994). Bounded anisotropy fluid model for ion temperatures. *Journal of Geophysical Research*, *99*(A6), 11225–11241. https://doi.org/10.1029/94JA00272

Denton, R. E., Anderson, B. J., Ho, G., & Hamilton, D. C. (1996). Effects of wave superposition on the polarization of electromagnetic ion cyclotron waves. *Journal of Geophysical Research*, *101*(A11), 24869–24885. https://doi.org/10.1029/96JA02251

Denton, R. E., Gary, S. P., Anderson, B. J., Fuselier, S. A., & Hudson, M. K. (1994). Low-frequency magnetic fluctuation spectra in the magnetosheath and plasma depletion layer. *Journal of Geophysical Research*, *99*(A4), 5893–5901. https://doi.org/10.1029/93JA02729

Denton, R. E., Hudson, M. K., & Roth, I. (1992). Loss-cone-driven ion cyclotron waves in the magnetosphere. *Journal of Geophysical Research*, *97*(A8), 12093–12103. https://doi.org/10.1029/92JA00954

Denton, R. E., Jordanova, V. K., & Fraser, B. J. (2014). Effect of spatial density variation and O^+ concentration on the growth and evolution of electromagnetic ion cyclotron waves. *Journal of Geophysical Research: Space Physics*, *119*, 8372–8395. https://doi.org/10.1002/2014JA020384

Dunlop, M. W., Balogh, A., Glassmeier, K.-H., & Robert, P. (2002). Four-point cluster application of magnetic field analysis tools: The curlometer. *Journal of Geophysical Research*, *107*, 1384. https://doi.org/10.1029/2001JA005088

Dunlop, M. W., & Eastwood, J. P. (2008). The curlometer and other gradient based methods. In G. Paschmann & P. W. Daly (Eds.), *Multi-spacecraft analysis methods revisited, ISSI Scientific Reports Series* (Vol. 385, 8, pp. 17–26). Bern: Springer.

Dunlop, M. W., Southwood, D. J., Glassmeier, K.-H., & Neubauer, F. M. (1988). Analysis of multipoint magnetometer data. *Advances in Space Research*, *8*(9), 273–277. https://doi.org/10.1016/0273-1177(88)90141-X

Engebretson, M. J., Posch, J. L., Capman, N. S. S., Campuzano, N. G., Belik, P., Allen, R. C., et al. (2018). MMS, Van Allen Probes, GOES 13, and ground-based magnetometer observations of EMIC wave events before, during, and after a modest interplanetary shock. *Journal of Geophysical Research: Space Physics*, *123*(10), 8331–8357. https://doi.org/10.1029/2018JA025984

Engebretson, M. J., Posch, J. L., Wygant, J. R., Kletzing, C. A., Lessard, M. R., Huang, C. L., et al. (2015). Van Allen probes, NOAA, GOES, and ground observations of an intense EMIC wave event extending over 12 hours in MLT. *Journal of Geophysical Research: Space Physics*, *120*(7), 5465–5488. https://doi.org/10.1002/2015JA021227

Ergun, R. E., Tucker, S., Westfall, J., Goodrich, K. A., Malaspina, D. M., Summers, D., et al. (2016). The axial double probe and fields signal processing for the MMS mission. *Space Science Reviews*, *199*(1-4), 167–188. https://doi.org/10.1007/s11214-014-0115-x

Fuselier, S. A., Lewis, W. S., Schiff, C., Ergan, R., Burch, J. L., Petrinec, S. M., & Trattner, K. J., (2016). Magnetospheric multiscale science mission profile and operations. *Space Science Reviews*, *199*, 77–103. https://doi.org/10.1007/s11214-014-0087-x

Gary, S. P., Anderson, B. J., Denton, R. E., Fuselier, S. A., & McKean, M. E. (1994). A limited closure relation for anisotropic plasmas from the Earth's magnetosheath. *Physics of Plasmas*, *1*(5), 1676–1683. https://doi.org/10.1063/1.870670

Gary, S. P., & Lee, M. A. (1994). The ion cyclotron anisotropy instability and the inverse correlation between proton anisotropy and proton beta. *Journal of Geophysical Research*, *99*, 11297–11301. https://doi.org/10.1029/94JA00253

Gershman, D. J., Vinas, A. F., Dorelli, J. C., Boardsen, S. A., Avanov, L. A., Bellan, P. M., et al. (2017). Wave-particle energy exchange directly observed in a kinetic Alfvén-branch wave. *Nature Communications*, *8*, 14719. https://doi.org/10.1038/ncomms14719

Glassmeier, K.-H., Motschmann, U., Dunlop, M., Balogh, A., Acuna, M. H., Carr, C., et al. (2001). Cluster as a wave telescope – First results from the fluxgate magnetometer. *Annales Geophysicae*, *19*, 1439–1447. https://doi.org/10.5194/angeo-19-1439-2001

Gomberoff, L., & Neira, R. (1983). Convective growth rate of ion cyclotron waves in a $H^+ - He^+$ and $H^+ - He^+ - O^+$ plasma. *Journal of Geophysical Research*, *88*(A3), 2170–2174. https://doi.org/10.1029/JA088iA03p02170

Horne, R. B., & Thorne, R. M. (1997). Wave heating of He^+ by electromagnetic ion cyclotron waves in the magnetosphere: Heating near the H^+-He^+ bi-ion resonance frequency. *Journal of Geophysical Research*, *102*, 11457–11471. https://doi.org/10.1029/97JA00749

Hu, Y., Denton, R. E., & Johnson, J. R. (2010). Two-dimensional hybrid code simulation of electromagnetic ion cyclotron waves of multi-ion plasmas in a dipole magnetic field. *Journal of Geophysical Research*, *115*(A19), A09218. https://doi.org/10.1029/2009JA015158

Isenberg, P. A. (1984). Resonant acceleration and heating of solar wind ions: Anisotropy and dispersion. *Journal of Geophysical Research*, *89*(A8), 6613–6622. https://doi.org/10.1029/JA089iA08p06613

Jackson, J. D. (1999). *Classical electrodynamics* (3rd ed.). New York, NY: Wiley.

Johnson, J. R., & Cheng, C. Z. (1999). Can ion cyclotron waves propagate to the ground? *Geophysical Research Letters*, *26*, 671–674.

Jordanova, V. K., Albert, J., & Miyoshi, Y. (2008). Relativistic electron precipitation by EMIC waves from self-consistent global simulations. *Journal of Geophysical Research*, *113*(A3), A00A10. https://doi.org/10.1029/2008JA013239

Kennel, C. F., & Petschek, H. E. (1966). Limit on stably trapped particle fluxes. *Journal of Geophysical Research*, *71*(1), 1–28. https://doi.org/10.1029/JZ071i001p00001

Kim, E.-H., & Johnson, J. R. (2016). Full-wave modeling of EMIC waves near the He$^+$ gyrofrequency. *Geophysical Research Letters*, *42*, 13–21. https://doi.org/10.1002/2015GL066978

Kim, E.-H., Johnson, J. R., Valeo, E., & Phillips, C. K. (2015). Global modeling of ULF waves at Mercury. *Geophysical Research Letters*, *42*, 5147–5154. https://doi.org/10.1002/2015GL064531

King, J. H., & Papitashvili, N. E. (1994). *Interplanetary medium data book, Supplement 5, 1988–1993, NSSDC/WDC-A-R&S 94-08*. Greenbelt, MA: NASA/National Space Science Data Center, GSFC.

Kitamura, N., Kitahara, M., Shoji, M., Miyoshi, Y., Hasegawa, H., Nakamura, S., et al. (2018). Direct measurements of two-way wave-particle energy transfer in a collision less space plasma. *Science*, *361*(6406), 1000–1003. https://doi.org/10.1126/science.aap8730

Kozyra, J. U., Cravens, T. E., Nagy, A. F., Fontheim, E. G., & Ong, R. S. B. (1984). Effects of energetic heavy ions on electromagnetic ion cyclotron wave generation in the plasmapause region. *Journal of Geophysical Research*, *89*(A4), 2217–2233. https://doi.org/10.1029/JA089iA04p02217

Lee, D.-Y., Shin, D.-K., & Choi, C.-R. (2018). Effects of oblique wave normal angle and noncircular polarization of electromagnetic ion cyclotron waves on the pitch angle scattering of relativistic electrons. *Journal of Geophysical Research: Space Physics*, *123*(6), 4556–4573. https://doi.org/10.1029/2018JA025342

Lee, J. H., & Angelopoulos, V. (2014). Observations and modeling of EMIC wave properties in the presence of multiple ion species as function of magnetic local time. *Journal of Geophysical Research: Space Physics*, *119*, 8942–8970. https://doi.org/10.1002/2014JA020469

Lee, J. H., Turner, D. L., Redondo, S. T., Vines, S. K., Allen, R. C., Fuselier, S. A., et al. (2019). MMS measurements and modeling of peculiar electromagnetic ion cyclotron waves. *Geophysical Research Letters*, *46*(21), 11622–11631. https://doi.org/10.1029/2019GL085182

Lindqvist, P.-A., Olsson, G., Torbert, R. B., King, B., Granoff, M., Rau, D., et al. (2016). The spin-plane double probe electric field instrument for MMS. *Space Science Reviews*, *199*(1–4), 137–165. https://doi.org/10.1007/s11214-014-0116-9

Mauk, B. H., & McPherron, R. L. (1980). An experimental test of the electromagnetic ion cyclotron instability within the Earth's magnetosphere. *Physics of Fluids*, *23*(10), 2111–2127. https://doi.org/10.1063/1.862873

Means, J. D. (1972). Use of the three-dimensional covariance matrix in analyzing the polarization properties of plane waves. *Journal of Geophysical Research*, *77*(28), 5551–5559. https://doi.org/10.1029/JA077i028p05551

Min, K., Denton, R. E., Liu, K., Gary, S. P., & Spence, H. E. (2017). Ion Bernstein instability as a possible source for oxygen ion cyclotron harmonic waves. *Journal of Geophysical Research: Space Physics*, *122*(5), 5449–5465. https://doi.org/10.1002/2017JA023979

Min, K., Lee, J., Keika, K., & Li, W. (2012). Global distribution of EMIC waves derived from THEMIS observations. *Journal of Geophysical Research*, *117*(A5), A05219. https://doi.org/10.1029/2012JA017515

Pakhotin, I. P., Walker, S. N., Shprits, Y. Y., & Balikhin, M. A. (2013). Dispersion relation of electromagnetic ion cyclotron waves using cluster observations. *Annales Geophysicae*, *31*(8), 1437–1446. https://doi.org/10.5194/angeo-31-1437-2013

Pinçon, J.-L., & Glassmeier, K.-H. (2008). Multi-spacecraft methods of wave field characterization. In G. Paschmann & P. W. Daly (Eds.), *Multi-spacecraft analysis methods revisited, ISSI Scientific Reports Series* (Vol. 8, pp. 47–54). Bern: Springer.

Pinçon, J.-L., & Motschmann, U. (1998). Multi-spacecraft filtering: General framework. In G. Paschmann & P. W. Daly (Eds.), *Analysis methods for multi-spacecraft data, ISSI Scientific Reports Series* (Vol. 1, pp. 65–78). Bern: Springer.

Pollock, C. J., Moore, T., Jacques, A., Burch, J., Gliese, U., Saito, Y., et al. (2016). Fast plasma investigation for magnetospheric multiscale. *Space Science Reviews*, *199*(1–4), 331–406. https://doi.org/10.1007/s11214-016-0245-4

Rauch, J. L., & Roux, A. (1982). Ray tracing of ULF waves in a multicomponent magnetospheric plasma: Consequences for the generation mechanism of ion cyclotron waves. *Journal of Geophysical Research*, *87*(A10), 8191–8198. https://doi.org/10.1029/JA087iA10p08191

Robert, P., Dunlop, M. W., Roux, A., & Chanteur, G. (1998). Accuracy of current density determination. In G. Paschmann & P. W. Daly (Eds.), *Analysis methods for multi-spacecraft data, ISSI scientific Reports Series* (Vol. 1, pp. 395–418). Bern: Springer.

Ronnmark, K. (1982). *Waves in homogeneous, anisotropic, multicomponent plasmas* (Technical Report Kiruna Geophys. Inst. Rep. 179, p. 56). Umea: Swedish Institute of Space Physics, Univeristy of Umea.

Russell, C. T., Anderson, B. J., Baumjohann, W., Bromund, K. R., Dearborn, D. T., Fischer, D., et al. (2016). The magnetospheric multiscale magnetometers. *Space Science Reviews*, *199*, 189–256. https://doi.org/10.1007/s11214-014-0057-3

Russell, C. T., Luhmann, J. G., & Strangeway, R. J. (2016). *Space physics: An introduction*. Cambridge, MA: Cambridge University Press.

Samson, J. C., & Olson, J. V. (1980). Some comments on the description of the polarization states of waves. *Geophysical Journal of the Royal Astronomical Society*, *61*(1), 115–129. https://doi.org/10.1111/j.1365-246X.1980.tb04308.x

Stix, T. H. (1992). *Waves in plasmas*. New York, NY: Springer.

Summers, D., & Thorne, R. M. (2003). Relativistic electron pitch angle scattering by electromagnetic ion cyclotron waves during geomagnetic storms. *Journal of Geophysical Research*, *108*, 1143. https://doi.org/10.1029/2002JA009489

Thorne, R. M. (2010). Radiation belt dynamics: The importance of wave-particle interactions. *Geophysical Research Letters*, *37*, L22107. https://doi.org/10.1029/2010GL044990

Thorne, R. M., & Horne, R. B. (1994). Energy transfer between energetic ring current H$^+$ and O$^+$ by electromagnetic ion cyclotron waves. *Journal of Geophysical Research*, *99*(A9), 17275–17282. https://doi.org/10.1029/94JA01007

Thorne, R. M., & Kennel, C. F. (1971). Relativistic electron precipitation during magnetic storm main phase. *Journal of Geophysical Research*, *76*, 4446–4453. https://doi.org/10.1029/JA076i019p04446

Toledo-Redondo, S., Lavraud, B., Fuselier, S. A., Andre, M., Khotyaintsev, Y. V., Nakamura, R., et al. (2019). Electrostatic spacecraft potential structure and wake formation effects for characterization of cold ion beams in the Earth's magnetosphere. *Journal of Geophysical Research: Space Physics*, *124*(12), 10048–10062. https://doi.org/10.1029/2019JA027145

Torbert, R. B., Burch, j. L., Giles, B. L., Gershman, D., Pollock, C. J., Dorelli, J., et al. (2016). Estimates of terms in Ohm's law during an encounter with an electron diffusion region. *Geophysical Research Letters*, *43*, 5918–5925. https://doi.org/10.1002/2016GL069553

Tsyganenko, N. A. (2002a). A model of the magnetosphere with a dawn-dusk asymmetry, 1, mathematical structure. *Journal of Geophysical Research*, *107*(A8), 1–15. https://doi.org/10.1029/2001JA000219

Tsyganenko, N. A. (2002b). A model of the near magnetosphere with a dawn-dusk asymmetry, 2, parameterization and fitting to observations. *Journal of Geophysical Research*, *107*(A8), 1–17. https://doi.org/10.1029/2001JA000220

Turner, D. L., Lee, J. H., Claudepierre, S. G., Fenell, J. F., Blake, J. B., Jaynes, A. N., et al. (2017). Examining coherency scales, substructure, and propagation of whistler mode chorus elements with Magnetospheric Multiscale (MMS). *Journal of Geophysical Research: Space Physics*, *122*(11), 11201–11226. https://doi.org/10.1002/2017JA024474

Ukhorskiy, A. Y., Shprits, Y. Y., Anderson, B. J., Takahashi, K., & Thorne, R. M. (2010). Rapid scattering of radiation belt electrons by storm-time EMIC waves. *Geophysical Research Letters*, *37*, L09101. https://doi.org/10.1029/2010GL042906

Vines, S. K., Allen, R. C., Anderson, B. J., Engebretson, M. J., Fuselier, S. J., Russell, C. T., et al. (2019). EMIC waves in the outer magnetosphere: Observations of an off-equator source region. *Geophysical Research Letters*, *46*(11), 5707–5716. https://doi.org/10.1029/2019GL082152

Wang, B., Su, Z., Zhang, Y., Shi, S., & Wang, G. (2016). Nonlinear Landau resonant scattering of near equatorially mirroring radiation belt electrons by oblique EMIC waves. *Geophysical Research Letters*, *43*, 3628–3636. https://doi.org/10.1002/2016GL068467

Wang, X. Y., Huang, S. Y., Allen, R. C., Fu, H. S., Deng, X. H., Zhou, M., et al. (2017). The occurrence and wave properties of EMIC waves observed by the Magnetospheric Multiscale (MMS) mission. *Journal of Geophysical Research: Space Physics*, *122*, 8228–8240. https://doi.org/10.1002/2017JA024237

Yahnin, A. G., & Yahnina, T. A. (2007). Energetic proton precipitation related to ion–cyclotron waves. *Journal of atmospheric and solar-terrestrial physics*, *69*(14), 1690–1706. https://doi.org/10.1016/j.jastp.2007.02.010

Young, D. T., Burch, J. L., Gomez, R. G., Santos, A. D. L., Miller, G. P., Wilson, P., et al. (2016). Hot plasma composition analyzer for the magnetospheric multiscale mission. *Space Science Reviews*, *199*, 407. https://doi.org/10.1007/s11214-014-0119-6

Yuan, Z., Liu, K., Yu, X., Yao, F., Huang, S., Wang, D., & Ouyang, Z. (2018). Precipitation of radiation belt electrons by EMIC waves with conjugated observations of NOAA and Van Allen satellites. *Geophysical Research Letters*, *45*, 12694–12702. https://doi.org/10.1029/2018GL080481

Zhang, J. -C., Kistler, L. M., Mouikis, C. G., Dunlop, M. W., Klecker, B., & Sauvaud, J.-A. (2010). A case study of EMIC wave-associated He$^+$ energization in the outer magnetosphere: Cluster and Double Star 1 observations. *Journal of Geophysical Research*, *115*, A06212. https://doi.org/10.1029/2009JA014784

Zhao, C., Russell, C. T., Strangeway, R. J., Petrinec, S. M., Paterson, W. R., Zhao, M., et al. (2016). Force balance at the magnetopause determined with MMS: Application to flux transfer events. *Geophysical Research Letters*, *43*(23), 11941–11947. https://doi.org/10.1002/2016GL071568